














## Use the 4S (Signal-Safe Speckle Subtraction): Explainable Machine Learning reveals the Giant Exoplanet AF Lep b in High-Contrast Imaging Data from 2011

MARKUS J. BONSE <sup>1,2</sup> TIMOTHY D. GEBHARD <sup>1,2,3</sup> FELIX A. DANNERT <sup>1,4</sup> OLIVIER ABSIL <sup>5</sup>  
FAUSTINE CANTALLOUBE <sup>6</sup> VALENTIN CHRISTIAENS <sup>5,7</sup> GABRIELE CUGNO <sup>1,8</sup> EMILY O. GARVIN <sup>1</sup>  
JEAN HAYOZ <sup>1</sup> MARKUS KASPER <sup>9</sup> ELISABETH MATTHEWS <sup>10</sup> BERNHARD SCHÖLKOPF <sup>2,11</sup> AND  
SASCHA P. QUANZ <sup>1,4</sup>

<sup>1</sup>ETH Zurich, Institute for Particle Physics & Astrophysics, Wolfgang-Pauli-Str. 27, 8093 Zurich, Switzerland

<sup>2</sup>Max Planck Institute for Intelligent Systems, Max-Planck-Ring 4, 72076 Tübingen, Germany

<sup>3</sup>Max Planck ETH Center for Learning Systems, Max-Planck-Ring 4, 72076 Tübingen, Germany

<sup>4</sup>National Center of Competence in Research PlanetS<sup>a</sup>

<sup>5</sup>University of Liège, STAR Institute, Allée du Six Août 19C, 4000 Liège, Belgium

<sup>6</sup>Université Grenoble Alpes, CNRS, IPAG, 38000 Grenoble, France

<sup>7</sup>KU Leuven, Institute for Astronomy, Celestijnenlaan 200D, Leuven, Belgium

<sup>8</sup>University of Michigan, Department of Astronomy, Ann Arbor, MI 48109, USA

<sup>9</sup>European Southern Observatory, Garching bei München, Germany

<sup>10</sup>Max Planck Institute for Astronomy, Königstuhl 17, 69117 Heidelberg, Germany

<sup>11</sup>Department of Computer Science, ETH Zurich, 8092 Zurich, Switzerland

### ABSTRACT

The main challenge of exoplanet high-contrast imaging (HCI) is to separate the signal of exoplanets from their host stars, which are many orders of magnitude brighter. HCI for ground-based observations is further exacerbated by speckle noise originating from perturbations in the Earth’s atmosphere and imperfections in the telescope optics. Various data post-processing techniques are used to remove this speckle noise and reveal the faint planet signal. Often, however, a significant part of the planet signal is accidentally subtracted together with the noise. In the present work, we use explainable machine learning to investigate the reason for the loss of the planet signal for one of the most used post-processing methods: Principal Component Analysis (PCA). We find that PCA learns the shape of the telescope point spread function for high numbers of PCA components. This representation of the noise captures not only the speckle noise, but also the characteristic shape of the planet signal. Building upon these insights, we develop a new post-processing method (4S) that constrains the noise model to minimize this signal loss. We apply our model to 11 archival HCI datasets from the VLT-NACO instrument in the L’-band and find that our model consistently outperforms PCA. The improvement is largest at close separations to the star ( $\leq 4 \lambda/D$ ) providing up to 1.5 magnitudes deeper contrast. This enhancement enables us to detect the exoplanet AF Lep b in data from 2011, 11 years before its subsequent discovery. We present updated orbital parameters for this object.

*Keywords:* Direct imaging (387), Astronomy data reduction (1861), Exoplanets (498), Interdisciplinary astronomy (804), High angular resolution (2167), Astronomy image processing (2306)

### 1. INTRODUCTION

The primary challenge of exoplanet high contrast imaging (HCI) is to separate and detect the light of faint exoplanets from their host stars, which are many orders

of magnitude brighter. During an observation, the light of the star gets scattered in the image plane, creating a halo of highly structured *speckle noise* superimposed on the planet signal. Speckles tend to mimic the expected shape of the planet, which makes it difficult to distinguish them from a real planet signal. There are two types of speckle noise (Males et al. 2021): *quasi-static speckles*, caused by nanometer scale imperfections in the telescope optics, and *atmospheric speckles*, resulting from the turbulence of the Earth’s atmosphere. Over the last

Corresponding author: Markus J. Bonse  
mbonse@phys.ethz.ch

<sup>a</sup> [www.nccr-planets.ch](http://www.nccr-planets.ch)

decade, considerable efforts have been spent to push the limits of HCI observations and reduce speckle noise. In this context, one key aspect is the development of faster and more accurate *eXtreme* Adaptive Optics (XAO) systems. Examples of such systems are the *Gemini Planet Imager* (GPI), the *Spectro-Polarimetric High-contrast Exoplanet REsearch instrument* (SPHERE), the *Subaru Coronagraphic Extreme Adaptive Optics* (SCEXAO) and MagAO-X (Macintosh et al. 2014; Jovanovic et al. 2015; Males et al. 2018; Beuzit et al. 2019). XAO uses new detectors, advanced wavefront sensors and deformable mirrors with higher actuator counts, along with faster computing hardware and control software. For HCI, they are often coupled with different types of coronagraphs to efficiently suppress the stellar point spread function (PSF) (Kenworthy et al. 2007; Mawet et al. 2009; Snik et al. 2012; N’Diaye et al. 2015; Otten et al. 2017).

Equally crucial for achieving deeper contrast and for removing speckle noise is the development of post-processing techniques (see Cantalloube et al. 2021, for an overview). Post-processing techniques are combined with dedicated observing strategies like angular differential imaging (ADI) (Marois et al. 2006), spectral differential imaging (SDI) (Racine et al. 1999; Sparks & Ford 2002), reference star differential imaging (RDI) (Mawet et al. 2012; Ruane et al. 2019) or polarimetric differential imaging (PDI) (Kuhn et al. 2001; Quanz et al. 2011) which are designed to enable planet signals to be distinguished from speckle noise. A major breakthrough for the processing of HCI data was the introduction of principal component analysis (PCA / KLIP; Amara & Quanz 2012; Soummer et al. 2012). Since its adoption to HCI, PCA has formed the basis for the analysis of many HCI surveys (Nielsen et al. 2019; Launhardt et al. 2020; Janson et al. 2021; Langlois et al. 2021; Cugno et al. 2023) and allowed the detection of several new planets (Macintosh et al. 2015; Chauvin et al. 2017).

However, after more than a decade of HCI observations, only a relatively small number of objects have been found (see Currie et al. 2023 for an overview and table of sub-stellar companions) and the results of several surveys have consistently shown that super-Jovian planets with masses between 5–13  $M_J$  at large separations (10–100 au) are extremely rare (between  $\sim 0.3$ –2.2% depending on stellar type; see Vigan et al. 2021). Only recently, taking advantage of the latest generation of instruments, it was possible to search for less massive planets at closer separations. While the sample size is still small, new planets have been detected in this regime (e.g., 51 Eri b; Macintosh et al. 2015, AF Lep b; Mesa et al. 2023; Franson et al. 2023; De Rosa et al. 2023) hinting at an elevated occurrence rate towards smaller masses and separations. On the other hand, radial velocity (RV) studies have found that the occurrence rate of giant planets peaks around  $3.6^{+2.0}_{-1.8}$  au, decreasing closer to the star and further out (Fulton et al. 2021). However, the decrease beyond 5–8 au has not been confirmed and

is still the subject of ongoing research (Lagrange et al. 2023). It is therefore crucial to push down the limits of HCI observations close to the star to bridge the gap and create an overlap between RV and HCI surveys. This will provide empirical access to an important parameter space for exoplanet population and formation models and allow for direct imaging follow-up of exoplanets detected by RV surveys.

Unfortunately, close to the star, it becomes increasingly difficult to suppress speckle noise using data post-processing techniques. If we use methods like PCA, a significant fraction of the planet signal is accidentally subtracted together with the noise. While at large separations the loss of planet signal is moderate, close to the star more than 95% of the planet signal might get lost (e.g., Gebhard et al. 2022; Bonse et al. 2023). This effect is referred to as planet over- and self-subtraction (Pueyo 2016) and represents the main bottleneck for post-processing of HCI data.

*Contributions:*—In this paper, we gain a deep understanding of the reason for the loss of planet signal in PCA and related methods and use it to develop a new post-processing algorithm. To this end, we revisit the mathematical background of PCA and give an overview of more recent post-processing methods in Section 2. By using methods from the field of explainable machine learning, we explore the reason for planet over- and self-subtraction (Section 3). We identify two main limitations of PCA, which we use as a basis to develop our new post-processing algorithm 4S (Section 4). A detailed analysis of the contrast performance of 4S on archival data from the VLT-NACO instrument is given in Section 5. We find that 4S reaches significantly deeper contrast at close separations to the star, and learns a model of the noise that matches our understanding of the speckle noise. Using 4S we can reveal the faint exoplanet AF Lep b in archival VLT-NACO data from 2011 (Section 6) which is not detectable with PCA. In Sections 7 and 8, we outline directions for future work and provide concluding remarks.

*Reproducibility:*—Along with this paper, we are releasing our algorithm 4S as a Python package called `fours`. The code is available on [GitHub](#) and comes with a documentation page on [ReadtheDocs](#). All raw data (Bonse 2024a) and intermediate results (Bonse 2024b) to reproduce our plots are available on [Zenodo](#).

## 2. PCA REVISITED

The concept of using PCA (or *Karhunen–Loève* transformation) in HCI is to estimate the stellar PSF and speckle noise to subtract it from the science data. For this purpose, PCA utilizes the temporal variability and brightness of the speckles. A typical HCI dataset consists of a sequence of individual exposures  $\mathbf{x}_{t,\text{raw}} \in \mathbb{R}^D$  with pixel resolution  $D = n_i \cdot n_j$  taken as a function of time  $t = 1, \dots, N$ . If we ignore background and detector

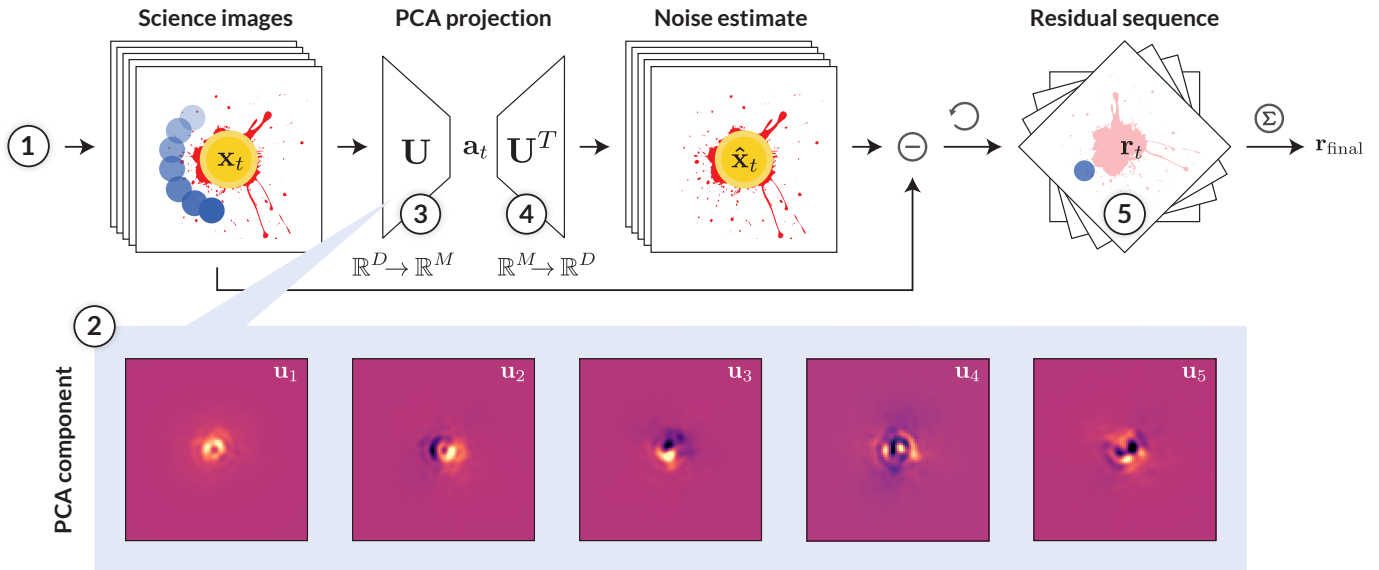


**Figure 1.** *Top row:* Illustration of how PCA is applied to ADI data in HCI. The planetary signal is shown in blue, while the stellar speckle noise is represented by the red splash. Details about the steps (①) to (⑤) are given in the text. *Bottom row:* Examples of the first 5 principal components are shown, estimated for the dataset #5 (HD 22049) in Table 1. Further details on the data are given in Section 5. The first components of PCA are often interpretable. For example,  $\mathbf{u}_1$  in the given example models the overall brightness variations of the post-coronagraphic PSF. The components  $\mathbf{u}_2$  and  $\mathbf{u}_3$  represent horizontal and vertical variations caused by small errors in the centering of the star behind the coronagraph.

noise, each image is composed of light from the star  $\mathbf{s}_t$  and possibly light from the planet  $\mathbf{p}_t$ :

$$\mathbf{x}_{t,\text{raw}} = \mathbf{s}_t + \mathbf{p}_t. \quad (1)$$

The stellar light  $\mathbf{s}_t$  outshines the planet signal  $\mathbf{p}_t$  by several orders of magnitude. As we go through the temporal stack of science images, the PSF and speckle pattern changes. This means that the strongest brightness variations in the data are due to the light of the star and not due to the planet. This data characteristic is the foundation of speckle-subtraction with PCA: PCA is a linear method which tries to find a low-dimensional representation of the data with dimension  $K \ll D$ , which only captures the strong covariances of the data. If the planet signal is weak compared to the speckle noise, it should thus not be part of this low-dimensional representation. If we reconstruct the data from the low-dimensional space, we get an estimate of the speckle noise that can be subtracted from the science data. Applying PCA to HCI data involves the following steps (see Figure 1):

- ① **Data preparation:** The temporal average of the science data  $\bar{\mathbf{x}}$  is subtracted from each individual science frame:

$$\mathbf{x}_t = \mathbf{x}_{t,\text{raw}} - \bar{\mathbf{x}}.$$

The mean subtracted 2D science frames are then flattened into one dimensional vectors and stacked

into a data matrix  $\mathbf{X} \in \mathbb{R}^{N \times D}$ :

$$\mathbf{X} = \begin{bmatrix} \mathbf{x}_1^T \\ \mathbf{x}_2^T \\ \vdots \\ \mathbf{x}_N^T \end{bmatrix} = \begin{bmatrix} x_{1,1} & x_{1,2} & \dots & x_{1,D} \\ x_{2,1} & x_{2,2} & \dots & x_{2,D} \\ \vdots & \vdots & \dots & \vdots \\ x_{N,1} & x_{N,2} & \dots & x_{N,D} \end{bmatrix}.$$

Each row in  $\mathbf{X}$  corresponds to one mean subtracted science frame.<sup>1</sup>

- ② **Calculation of the projection matrix:** We choose the dimensionality of the low-dimensional space  $K$  and calculate the PCA basis (i.e., the projection matrix  $\mathbf{U} \in \mathbb{R}^{D \times K}$ ) which transforms our data into the low-dimensional space:

$$\mathbf{U} = [\mathbf{u}_1 \dots \mathbf{u}_K].$$

The column vectors of  $\mathbf{U}$  are the principal components  $\mathbf{u}_1, \dots, \mathbf{u}_K, \forall \mathbf{u} \in \mathbb{R}^D$ . Details on how to calculate these components are given in the next section.

<sup>1</sup> We choose the notation to be consistent with our Python implementation. Our notation might deviate from the conventions used in other papers (e.g., Lewis et al. 2023).

- ③ **Dimensionality reduction:** We project our data into the low dimensional space  $\mathbf{x}_t \rightarrow \mathbf{a}_t$ ,  $\mathbf{a}_t \in \mathbb{R}^K$ :

$$\mathbf{X} \cdot \mathbf{U} = \begin{bmatrix} \mathbf{a}_1^T \\ \mathbf{a}_2^T \\ \vdots \\ \mathbf{a}_N^T \end{bmatrix} = \mathbf{A} \in \mathbb{R}^{N \times K}. \quad (2)$$

If the dimensionality  $K$  is chosen carefully, the low-dimensional representation  $\mathbf{A}$  should mostly capture the variations caused by the star.

- ④ **Data reconstruction:** We reconstruct our data from the low-dimensional space  $\mathbf{a}_t \rightarrow \hat{\mathbf{x}}_t$ ,  $\hat{\mathbf{x}}_t \in \mathbb{R}^D$ :

$$\mathbf{A} \cdot \mathbf{U}^T = \begin{bmatrix} \hat{\mathbf{x}}_1^T \\ \hat{\mathbf{x}}_2^T \\ \vdots \\ \hat{\mathbf{x}}_N^T \end{bmatrix} = \hat{\mathbf{X}}.$$

Since  $\mathbf{a}_t$  mostly captures the strong covariances of the data, we can use its reconstruction to approximate the speckle noise:

$$\hat{\mathbf{x}}_t \approx \mathbf{s}_t. \quad (3)$$

- ⑤ **Calculation of the residual:** We subtract the noise estimate  $\hat{\mathbf{x}}_t$  for each mean-subtracted science frame  $\mathbf{x}_t$ . In the case of angular differential imaging (ADI; Marois et al. 2006), we have to de-rotate all frames such that North is up in all images. The result is the so-called residual sequence  $\mathbf{r}_t$ :

$$\mathbf{r}_t = \phi_t(\mathbf{x}_t - \hat{\mathbf{x}}_t), \quad (4)$$

where  $\phi_t$  is the de-rotation function, which uses the parallactic angles to re-align North in all images. The final residual image  $\mathbf{r}_{\text{final}}$  can then be obtained by averaging along the time axis:<sup>2</sup>

$$\mathbf{r}_{\text{final}} = \frac{1}{N} \sum_{t=1}^N \mathbf{r}_t. \quad (5)$$

### 2.1. How to find the optimal projection?

Depending on the type of the dataset, the projection matrix  $\mathbf{U}$  can be calculated based on the science data directly (e.g., in case of ADI, Amara & Quanz 2012; Soummer et al. 2012) or based on reference stars (RDI, Ruane et al. 2019). In this work, we focus on ADI,

but the same concepts apply for RDI. As motivated in the previous section, we want to choose  $\mathbf{U}$  such that the strongest variations of the data, that is, the speckle noise, are captured in the low-dimensional space. This objective is equivalent to the maximum variance derivation of PCA (see, e.g., chapter 12.1 of Bishop 2006 for the details).

For simplicity, let us consider the projection onto the first component  $\mathbf{u}_1$ . We want to choose  $\mathbf{u}_1$  such that the variance along the first axis of the low-dimensional space  $\sigma^2(a_{t,1})$  is large:

$$\sigma^2(a_{t,1}) = \mathbf{u}_1^T \mathbf{C} \mathbf{u}_1,$$

where  $\mathbf{C} \in \mathbb{R}^{D \times D}$  is the covariance matrix of the data

$$\mathbf{C} = \frac{1}{T} \mathbf{X}^T \mathbf{X}.$$

We add another constraint  $\|\mathbf{u}_1\| = \mathbf{u}_1^T \mathbf{u}_1 = 1$  to avoid  $\|\mathbf{u}_1\| \rightarrow \infty$ . To enforce this constraint, we introduce a Lagrange multiplier  $\lambda_1$  which gives us the following optimization objective:

$$\arg \max_{\mathbf{u}_1} = \mathbf{u}_1^T \mathbf{C} \mathbf{u}_1 + \lambda_1 (1 - \mathbf{u}_1^T \mathbf{u}_1).$$

If we set the derivative w. r. t.  $\mathbf{u}_1$  equal to zero, we get:

$$\mathbf{C} \mathbf{u}_1 = \lambda_1 \mathbf{u}_1.$$

This means that  $\mathbf{u}_1$  should be chosen to be an eigenvector of  $\mathbf{C}$ . Using  $\mathbf{u}_1^T \mathbf{u}_1 = 1$  we see that:

$$\sigma^2(a_{t,1}) = \mathbf{u}_1^T \mathbf{C} \mathbf{u}_1 = \lambda_1.$$

To maximize the variance of the projection, we should therefore choose the eigenvector  $\mathbf{u}$  with the largest eigenvalue. We sort all eigenvectors of  $\mathbf{C}$  by their eigenvalues:

$$\begin{matrix} \lambda_1 & > & \lambda_2 & > & \dots & > & \lambda_K & > & \dots & > & \lambda_D \\ \mathbf{u}_1 & & \mathbf{u}_2 & & \dots & & \mathbf{u}_K & & \dots & & \mathbf{u}_D \end{matrix},$$

and select the first  $K$  eigenvectors with the largest eigenvalues. In practice,  $\mathbf{U}$  is usually obtained by computing a singular value decomposition (SVD) of the data matrix  $\mathbf{X}$ . This approach ensures numerical stability and reduces computation time.

A big advantage of PCA is that the first components of the matrix  $\mathbf{U}$  can be interpreted visually (see Figure 1). For example, the first component  $\mathbf{u}_1$  often models the general brightness variations of the stellar PSF. The data used to calculate the components in Figure 1 was taken with a vortex coronagraph (Mawet et al. 2013). Thus, the first component shows the typical donut-shape of the post-coronagraphic PSF. The second and third components show the response of the coronagraphic PSF to tip-tilt errors (i.e., the first modes of the AO).

<sup>2</sup> Some implementations take the median along time instead of the mean, which can be advantageous in the case of detector artifacts such as bad pixels.

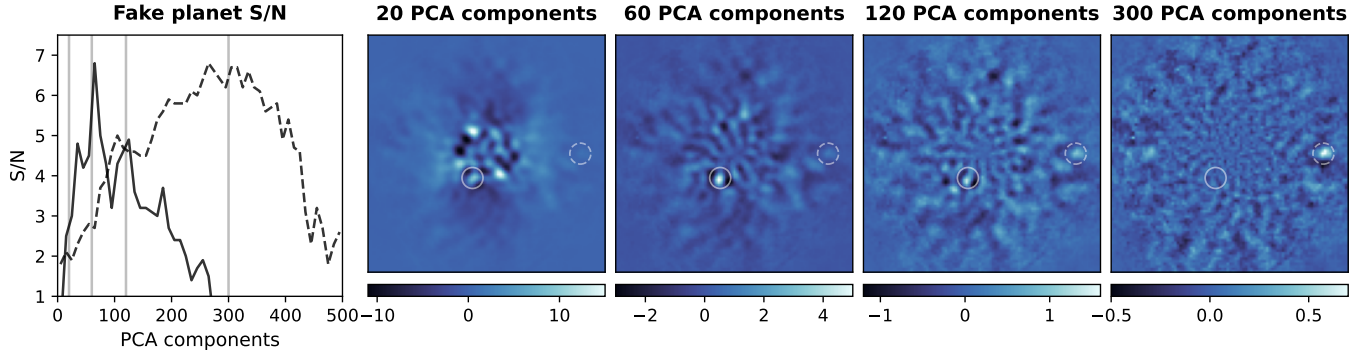


**Figure 2.** Variation in planet visibility as a function of principal components ( $K = 20$ ,  $K = 60$ ,  $K = 120$ ,  $K = 300$ ). The shown dataset is dataset #5 (HD 22049) in Table 1. More details on data pre-processing are given in Section 5. Two fake planets have been inserted into the data: one positioned at  $\sim 3 \lambda/D$  separation from the star with a contrast brightness of 9 mag (white circle), and one at  $\sim 10 \lambda/D$  with a contrast brightness of 12.5 mag (white dashed circle). The inner planet reaches the highest S/N at  $\sim K = 60$  components (left plot, solid line) and the outer planet at  $\sim K = 300$  components (left plot, dashed line). This example highlights the challenge of choosing the right number of principal components within a single dataset.

### 2.2. Limitations of PCA

PCA is widely used by the exoplanet imaging community and available in most HCI packages such as VIP (Christiaens et al. 2023), PynPoint (Stolker et al. 2019) or pyKLIP (Wang et al. 2015). Its appeal is mainly due to its simplicity and to the fact that it comes with only a single hyperparameter: the number of principal components  $K$ . However, this apparent simplicity hides a complex interplay of several factors which makes it difficult to tune  $K$  in practice. The optimal choice is highly dataset-specific, influenced by variables such as the instrument, observing mode, wavelength, and observing conditions. Even within a single dataset, the optimal number of components can vary as a function of the separation from the star (Meshkat et al. 2013). This is to be expected, as low order wavefront modes, which affect the closest separations to the star, vary the most. The further away from the center, the higher the modal order and the larger the required  $K$ . An example of this effect is shown in Figure 2. Two artificial planets are inserted into the same dataset: one close to the star ( $\sim 3 \lambda/D$ ) and another farther out ( $\sim 10 \lambda/D$ ). The closer planet is best seen if 60 principal components are selected, whereas the farther one requires about 300 components to be fully visible. Notably, at 300 components, the signal of the inner planet is completely lost. This demonstrates a critical limitation of PCA: as the number of components increases, PCA does not only model the noise but starts to include parts of the planet signal, leading to what is known as planet self- and over-subtraction (Pueyo 2016). As discussed further in Section 5, the choice of the number of components can affect the final contrast by several magnitudes. Hence, selecting the right number of components is crucial; it can be the difference between a detection and a non-detection.

### 2.3. Beyond PCA

The loss of planet signal in PCA has encouraged the development of more advanced post-processing techniques. Nevertheless, many of these methods either enhance PCA or incorporate its principles. Annular PCA, for instance, applies PCA in concentric annular segments around the star (Absil et al. 2013; Gomez Gonzalez et al. 2017). A specific exclusion criterion for ADI prevents the signal of the planet from entering the PCA basis. Lewis et al. (2023) extends PCA to utilize the temporal and spatial axis simultaneously.

After the speckle-subtraction the residual images are commonly analyzed with meta-techniques which quantify detections and non-detections; for example using  $t$ -tests (Mawet et al. 2014), STIM maps (Pairet et al. 2019) or performance maps (Jensen-Clem et al. 2017). A recent overview of these methods can be found in Bonse et al. (2023). Beyond the analysis of a single residual, supervised machine learning techniques have been proposed (Gomez Gonzalez et al. 2018; Cantero et al. 2023). These methods use several PCA residuals with different numbers of components as input and train a neural network to detect the planet. The RSM map by Dahlqvist et al. (2020) and Dahlqvist & Absil (2021) replaces the temporal averaging in the last step of PCA. It allows the combination of multiple PCA outputs alongside other post-processing techniques.

Conceptually similar to PCA are other subtraction-based techniques which replace the bottleneck of PCA (e.g., NNMF Arcidiacono & Simoncini 2018; Ren et al. 2018 or LLSG Gomez Gonzalez et al. 2016). For example, LLSG adds an extra sparse term to the model with the goal of limiting the inclusion of the planet in the noise model. Daglayan et al. (2023) propose to change the objective function to a L1 loss to account for the heavy-tailed distribution of the speckle noise. The recently proposed ConStruct method uses non-linear auto-encoders

to locally predict the speckle noise (Wolf et al. 2023). Further examples of subtraction-based techniques are LOCI and its variations (Lafrenière et al. 2007; Marois et al. 2014; Wahhaj et al. 2015; Thompson & Marois 2021), or the more recently proposed HSR (Gebhard et al. 2022). Bonse et al. (2018) proposed to use wavelets to reduce speckle noise in time. Most of these methods discuss different exclusion criteria to avoid subtraction of the planet signal.

Complementary to subtraction-based techniques are inverse-problem based methods. Instead of modeling and subtracting the noise, these methods rely on forward-modeling to search for the expected signature of planets in the data. Examples are ANDROMEDA (Cantalloube et al. 2015), FMMF (Pueyo 2016; Ruffio et al. 2017), PACO (Flasseur et al. 2018, 2024) and TRAP (Samland et al. 2021). In this context, FMMF is the direct extension of PCA to forward-modeling.

Although the concepts behind these modern post-processing techniques are diverse, they share the common idea of better using the knowledge about the shape and behavior of the planet signal. However, despite all these efforts, PCA still represents the main benchmark in practice: For example, Franson et al. (2023) used it for the discovery of the exoplanet AF Lep b. Further, none of these advanced algorithms have managed to completely avoid the problem of planet signal loss, which is the main bottleneck for achieving deeper detection limits.

### 3. EXPLAINING SIGNAL LOSS IN PCA

In the previous section, we observed that with an increasing number of principal components, progressively more signal of the planet is lost. Is there a specific component responsible for this effect? While the first components of PCA can be interpreted visually (Figure 1), it is difficult to understand the higher order modes. To better understand why we lose signal in PCA, we propose to use methods from the field of eXplainable Artificial Intelligence (XAI). With the recent boom in machine learning, there is a trend towards increasingly complex deep network architectures. Unfortunately, the decisions made by such models are hard to understand and therefore hard to trust. XAI seeks to gain a better understanding of *why* and *how* machine learning models make their decisions, thus giving us a glimpse into the black box. A large number of XAI methods have been proposed in the literature (see Ali et al. 2023, for a recent overview). Some of them are model-specific (e.g., tailored to neural networks), while other methods are more generally applicable (e.g., LIME by Ribeiro et al. 2016). In the following paragraph, we will keep our explanation of the XAI method used in the present paper general, to provide the basis for a better understanding of other post-processing methods beyond PCA.

#### 3.1. Saliency maps

A widely used approach to explain the predictions of machine learning methods is the use of input gradients. The most basic approach was proposed by Simonyan et al. (2013). It is often referred to as *Vanilla Gradient* and straightforward to apply to subtraction-based post-processing methods in HCI:

Let us consider a single science image  $\mathbf{x}_t$  at time  $t$ . Given a speckle-subtraction method  $S$ , we estimate the speckle noise for this particular image:

$$S(\mathbf{x}_t) = \hat{\mathbf{x}}_t.$$

For each pixel position in the noise estimate  $\hat{\mathbf{x}}_t$ , we can use input gradients to calculate so-called *saliency maps*. Saliency maps are heatmaps which highlight areas in the input image  $\mathbf{x}_t$  which contribute the most to the noise estimate at the selected pixel position. Given a pixel position, we calculate the derivative of  $S_{(i,j)}$  with respect to the input image  $\mathbf{x}$  at the point  $\mathbf{x}_t$ :

$$\mathbf{w} = \left. \frac{\partial S_{(i,j)}}{\partial \mathbf{x}} \right|_{\mathbf{x}_t}. \quad (6)$$

The magnitude of the derivative  $\mathbf{w}$  points to pixels in  $\mathbf{x}$  that cause the largest difference on the noise estimate at the position  $(i, j)$ . For each pixel position  $(i, j)$  in the noise estimate, we get the saliency map  $M_{(i,j)}$  by first calculating the input gradient using Equation (6), then rearranging the one-dimensional vector  $\mathbf{w}$  back into a two-dimensional image, and, finally, taking the absolute value:

$$M_{(i,j)} = |\mathbf{w}_{(i,j)}|$$

Saliency maps can be computed for any post-processing method  $S$  for which we can calculate the gradient in Equation (6). For non-linear methods such as ConStruct (Wolf et al. 2023) or SODINN (Gomez Gonzalez et al. 2018), more advanced methods such as SmoothGrad (Smilkov et al. 2017) or Integrated Gradients (Sundararajan et al. 2017) are likely to give better results than *Vanilla Gradients*.

#### 3.2. Right for the wrong reasons

In the case of PCA, the noise subtraction method  $S$  is just the projection onto the low-dimensional space and its reconstruction:

$$S_{\text{PCA}}(\mathbf{x}_t) = \mathbf{x}_t^T \mathbf{U} \mathbf{U}^T = \hat{\mathbf{x}}_t \quad (7)$$

Given the number of principal components  $K$ , we compute  $\mathbf{U}$  using the procedure explained in Section 2.1. Assuming that  $\mathbf{U}$  is fixed, the saliency map of PCA is then given by:

$$M_{(i,j),\text{PCA}} = |\mathbf{U} \mathbf{U}^T|_{[:,n_{ij}+i]} \quad (8)$$

Each pixel value in the noise estimate of PCA is a weighted sum of the pixel values in the science frame.

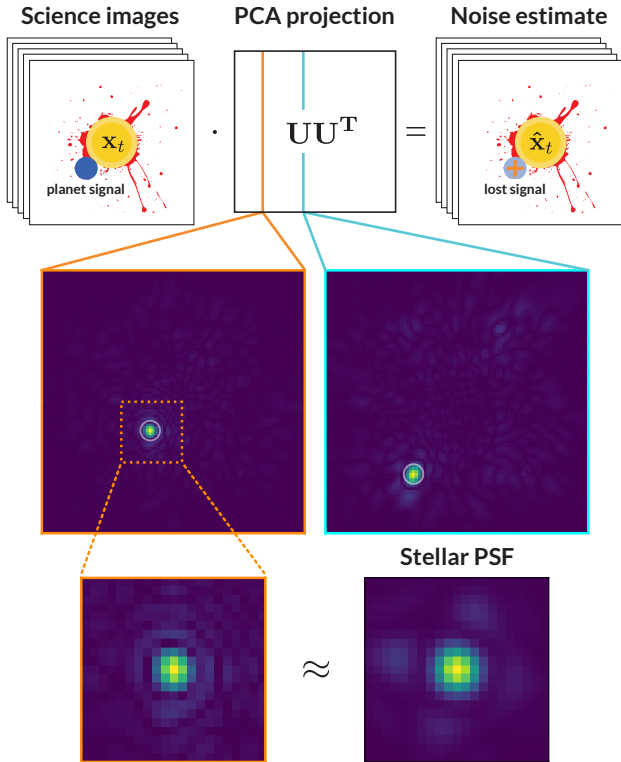


**Figure 3.** Illustration of how to compute saliency maps for PCA. For each pixel position in the noise estimate, we can compute one saliency map. Each saliency map highlights the areas in the science frame that are used to obtain the noise estimate at the respective position. Since the noise model of PCA is linear, every pixel in the noise estimate is a weighted sum of the pixels in the input image. The saliency map shows the absolute value of these weights. Two examples of such saliency maps are shown in the middle row (300 principal components). The example used in the text is marked in orange. For large numbers of principal components, the saliency map converges to the shape of the PSF. A gallery of saliency maps for different separations and number of principal components is given in Figure 14.

The weights of this sum are the column vectors of the matrix  $UU^T$ . This means that *each column* in  $UU^T$  gives us an explanation for which information is used to estimate the noise at *one output pixel position*. To get the saliency map for the pixel  $(i, j)$ , we have to select the  $(n_i j + i)$ -th column vector of  $UU^T$  and take its absolute value. Note that since PCA is a linear model, the saliency map for a given position is the same for all science frames along time.

Figure 3 illustrates the concept and provides examples of saliency maps for PCA based on dataset #4 (HD 22049) (see Section 5 for more details on the dataset). To better understand the loss of planet signal in PCA, let us assume that the planet signal in the science frame (Figure 3, top left image) is at the position marked

by the blue circle. If parts of the planet signal are lost in the subtraction step, it means that some signal leaks into the noise estimate at the same position (top right image, orange +). We can use Equation (8) to compute the saliency map for this position (Figure 3, middle row, left image). It turns out that most of the information used to estimate the noise at the planet’s position is only taken from the input image at the planet’s position. This means that PCA just copies the planet signal from the input image to the noise estimate. The same pattern can be observed for other pixel positions which do not contain the planet signal (Figure 3, middle row, right image). This means that even if the planet’s position changes as a function of time (e.g., in the case of ADI), it is still subtracted.

It is interesting to note that the shape of the information used corresponds to the shape of the unsaturated PSF. We know that, to first order, the speckles follow the shape of the PSF (i.e., discarding wavelength-smearing effects). This means that PCA successfully learns what the speckles look like. Since, not only the speckles follow the shape of the PSF, but also the signal of the planet, the latter is partially subtracted.

It should be noted that this problem occurs regardless of whether the planet is actually in the data. That is, even if we build the PCA basis using data from a different star (RDI), we still get a model that can subtract the planet signal. As the number of components increases, the projection  $UU^T$  converges to a *de facto* identity by learning the shape of the PSF. This convergence prevents us from learning more complex noise patterns.

*Quantification of the effect*—The convergence rate of PCA to the shape of the PSF is very dataset- and instrument-specific, and depends on whether the noise is dominated by speckles. For reasons explained later in Section 5, we confine our analysis to the VLT-NACO data taken in the  $L'$  filter, leaving research on other instruments for future work.

To quantify how many components are needed to converge to the shape of the PSF, we compute  $UU^T$  for different numbers of principal components  $K \in [1, \dots, 500]$ . We calculate saliency maps for pixel positions at  $1.5 \lambda/D$ ,  $4 \lambda/D$  and  $8 \lambda/D$ , and estimate the *match* between the saliency map and the unsaturated PSF template. More precisely, we compute a scalar product between the local saliency map and the unsaturated PSF and normalize it by the maximum value over all separations and components. The result of this experiment is shown in Figure 4. For separations close to the star, PCA converges much faster to the shape of the PSF than further out. This observation is in line with the fake planet experiment shown in Figure 2. While the signal of the fake planet close to the star is lost at 300 components, the planet further out is still clearly visible. The speckle intensity gradually decreases with separation from the star. As PCA models the strongest covariances first, the conver-

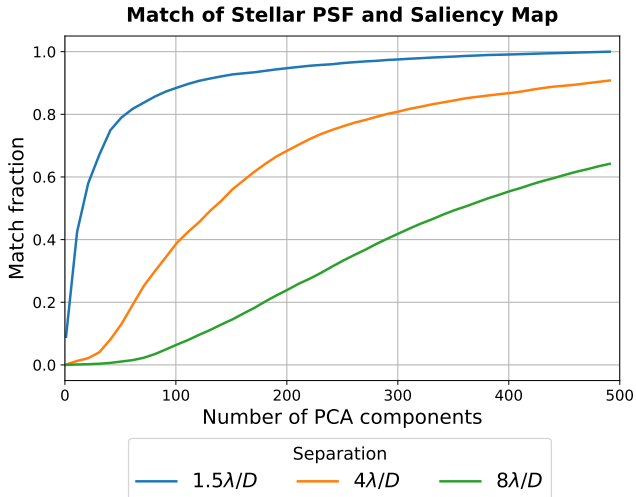


**Figure 4.** Convergence of the saliency map to the shape of the PSF as a function of the number of principal components used. At closer separations from the star, the convergence is faster, resulting in a greater loss of the planet signal with a smaller number of components.

gence to the shape of the PSF is faster close to the star. As a result, the risk of losing parts of the planet signal is also higher close to the star.

### 3.3. Misguided loss function

The origin of the planet signal loss described in the previous section occurs regardless of whether a planet signal is present in the data used to compute the PCA basis. It is therefore often referred to as planet over-subtraction. In the case of ADI datasets, in addition to over-subtraction, the planet signal can also directly affect the PCA basis. This second effect is known as planet self-subtraction and can lead to even greater signal loss. In Section 2.1, we explained how to derive PCA by maximizing the variance in the low-dimensional space. This derivation is well motivated for HCI, since the speckles are usually much brighter and more variable than the planet signal. An alternative derivation of PCA is the minimum reconstruction error formulation. We want to find a linear dimensionality reduction that minimizes the following reconstruction loss:

$$\mathcal{L}_{\text{PCA}} = \frac{1}{N} \sum_{t=1}^N \underbrace{\|\mathbf{x}_t - \hat{\mathbf{x}}_t\|^2}_{\mathbf{s}_t + \mathbf{p}_t - \hat{\mathbf{x}}_t}. \quad (9)$$

That is, we want our reconstruction  $\hat{\mathbf{x}}_t$  to be close to our science data  $\mathbf{x}_t$ . Both the maximum variance derivation and the minimum reconstruction error formulation yield the same algorithm (cf. chapter 12.1.2 in Bishop 2006). In the context of HCI, minimizing Equation (9) can be problematic, as  $\mathbf{x}_t$  contains both speckle noise and planet signal. This means that  $\mathcal{L}_{\text{PCA}}$  can only become small

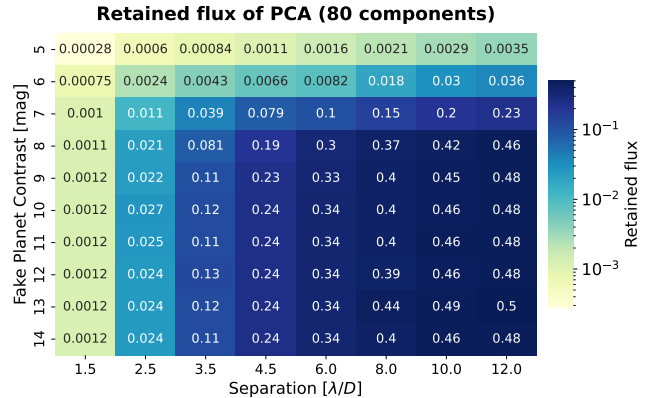


**Figure 5.** Retained flux after post-processing with PCA as a function of planet brightness and separation from the star. The grid was computed using `applefy`. Each value in the grid is the result of 3 fake planet experiments with planets inserted at different position angles. A significant fraction of the planet signal is lost, especially close to the star.

if the noise estimate  $\hat{\mathbf{x}}_t$  also fits the signal of the planet  $\mathbf{p}_t$ . For large numbers of principal components, and for bright companions, PCA tends to include the companion signal in its basis.

To quantify this effect, we compute a throughput grid using the Python package `applefy` (Bonse et al. 2023). A throughput grid illustrates the attenuation of the planet signal due to the data post-processing. The grid is computed by inserting fake companions with different known brightnesses and distances to the star, and then measuring the fraction of the flux that remains after PSF subtraction. The result of this experiment is shown in Figure 5. We observe that for faint companions the retained flux is only a function of the separation and does not depend on the brightness of the companion. This gradual loss of planet signal closer to the star is caused by the convergence of PCA to the shape of the PSF (see Section 3.2). For bright companions, however, PCA begins to include parts of the signal into its basis, causing an even greater loss of planet signal. The brightness at which planets are affected depends on the number of principal components. If more components are used, fainter companions start to be affected.

## 4. 4S: SIGNAL SAFE SPECKLE SUBTRACTION

In the previous section, we identified two main reasons for the loss of planet signal in PCA: first, the convergence of the noise model to the telescope’s PSF, and second, a problematic loss function that accidentally leads the noise estimate to fit the planet signal. Based on these findings, we propose a novel post-processing method that adopts the main steps of PCA but overcomes its limitations. We have named this method 4S, short for Signal Safe Speckle Subtraction. 4S is characterized by three innovations: First, a linear noise model with a *right reason* constraint, second, a new loss function that



is invariant to the planet signal, and third, a domain knowledge-informed regularization.

#### 4.1. The right reason constraint

In Section 3.2, we found that the noise model of PCA converges to a *de facto* identity that reproduces the shape of the telescope’s PSF. This is problematic as both the speckle noise and the planet signal follow this shape. Ideally, we would like our noise model to specifically recognize the speckle noise, that is, we want to find explanations for the speckle noise that are unique to the noise and do not describe the planet signal. In the context of XAI, Ross et al. (2017) proposed to add a *right reason* penalty to guide the predictions of neural networks using domain knowledge. The domain knowledge is represented as a mask that penalizes *wrong* explanations. The method has been successfully applied in practice (Schramowski et al. 2020). Inspired by this work, we propose a *right reason* constraint to prevent the noise model of 4S from learning the shape of the telescope’s PSF.

Like PCA (cf. Equation (7)), 4S uses a linear model, but its projection matrix  $\mathbf{B}$  is modified to circumvent the bottleneck of PCA:

$$4\mathbf{S}(\mathbf{x}_t) = \mathbf{x}_t^T \mathbf{B} = \hat{\mathbf{x}}_t \quad . \quad (10)$$

For PCA, each column of the projection matrix  $\mathbf{U}\mathbf{U}^T$  gives us an explanation of which information of the input  $\mathbf{x}_t$  is used to estimate the noise at one pixel position in  $\hat{\mathbf{x}}_t$ . Similarly, the columns of  $\mathbf{B} \in \mathbb{R}^{D \times D}$  contain the explanations of 4S. Following the idea of Ross et al. (2017), we limit the information of  $\mathbf{x}_t$  that can be used to predict the noise. For each pixel position in the noise estimate  $\hat{\mathbf{x}}_{(i,j)}$ , we have one parameter vector  $\beta_{(i,j)} \in \mathbb{R}^D$  as a column of  $\mathbf{B}$ . We design a circular *right reason* mask for each pixel position which sets the values near the *de facto* identity to zero:

$$\mathbf{B}_{[:,n_i+j+i]} = \beta_{(i,j)} \circ \mathbf{m}_{(i,j)},$$

where  $\circ$  is the element-wise multiplication. The right reason mask  $\mathbf{m}_{(i,j)}$  is defined as:<sup>3</sup>

$$\mathbf{m}_{(i,j)}(i', j') = \begin{cases} 0, & \text{if } \sqrt{(i-i')^2 + (j-j')^2} \leq d, \\ 1, & \text{otherwise} \end{cases}, \quad (11)$$

where  $d$  sets the radius of the mask. We choose  $d$  relative to the size of the PSF:  $d = 0.75 \cdot \text{FWHM}$ . This mask size ensures that the core of the PSF is protected from the *de facto* identity, while local information about the speckle noise is still preserved. A larger mask size allows us to protect even more signal, but also weakens the noise

model. The value of  $d = 0.75 \cdot \text{FWHM}$  is a compromise for which we have obtained good results in practice.

The right reason mask should not be confused with the exclusion criteria used by other post-processing techniques (e.g., Absil et al. 2013; Gomez Gonzalez et al. 2017; Lafrenière et al. 2007; Wahhaj et al. 2015). The mask does not block the signal of the planet, but instead forces the noise model to explore other areas of the input image that explain the speckle noise. Our approach is similar to the post-processing methods based on the HSR (Samland et al. 2021; Gebhard et al. 2022). However, while Gebhard et al. (2022) select areas in the input images that promise to contain useful information about the speckle noise, we use the entire science frame, but exclude areas that correspond to the shape of the telescope’s PSF near the *de facto* identity.

#### 4.2. Signal invariant loss function

A second limitation of PCA is its loss function (see Equation (9)), which can only become small if the noise estimate includes the planet signal. This is problematic in the case of ADI, for which the planet signal is part of the dataset used to compute the PCA basis. Different types of exclusion regions (Lafrenière et al. 2007; Cantalloube et al. 2015; Thompson & Marois 2021) or explicit planet models (Samland et al. 2021) have been proposed in the literature to protect the planet’s signal from becoming part of the noise estimate. These methods, however, often come with additional hyperparameters which are hard to optimize in practice. Therefore, instead of minimizing the reconstruction loss, as done in Equation (9), we propose to minimize the variance along the temporal axis in the de-rotated residual sequence:

$$\mathcal{L}_{4S} = \frac{1}{N} \sum_{t=1}^N \|\mathbf{r}_t - \bar{\mathbf{r}}\|^2, \quad \bar{\mathbf{r}} = \frac{1}{N} \sum_{t=1}^N \mathbf{r}_t. \quad (12)$$

An illustration of why  $\mathcal{L}_{4S}$  is sensitive to the speckle noise but does not affect the planet signal is shown in the bottom right box of Figure 6. In the de-rotated residual sequence  $\mathbf{r}_t$ , the signal of the planet  $\mathbf{p}_t$  is always at the same position and has approximately constant brightness<sup>4</sup>. Consequently, it only contributes to the temporal mean  $\bar{\mathbf{r}}$  but does not influence the temporal variance. Since the temporal mean  $\bar{\mathbf{r}}$  is subtracted in Equation (12), the loss function becomes invariant to the presence of the planet signal. Quasi-static and atmospheric speckles, however, vary with time, which is why they affect the loss function (red dashed line in Figure 6). Note that the noise model of 4S is still applied to the

<sup>3</sup> Note: The mask does not have to be binary, which is beneficial for datasets with low resolution. Our implementation makes use of circular apertures based on the `photutils` package.

<sup>4</sup> We do not account for changing conditions during the night. However, if information about the variability of the planet signal as a function of time is available (e.g., for data taken with a vAPP coronagraph such as in Otten et al. 2017), one could normalize for these variations as part of the pre-processing.

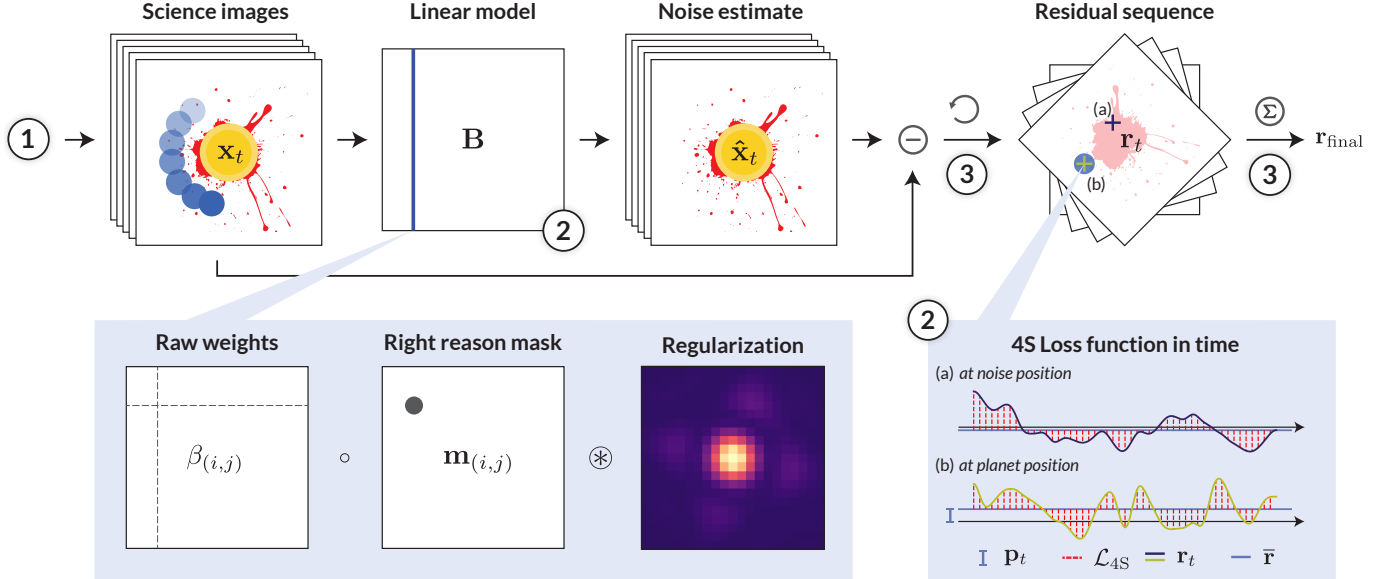


**Figure 6.** Illustration of our new post-processing technique 4S. To overcome the limitations of PCA, 4S makes use of three innovations: I. a *right reason* mask to prevent over-subtraction (bottom left box), II. a loss function which is invariant to the signal of the planet (bottom right box), and III. a regularization based on domain knowledge to prevent overfitting. The main steps ① to ③ are explained in detail in Section 4.4.

science images before de-rotation (cf. Equation (10)). Only the loss function is evaluated on the de-rotated residual sequence.

The signature of the noise learned by 4S is encoded in the projection matrix  $\mathbf{B} \in \mathbb{R}^{D \times D}$ , which contains the parameters  $\beta$  of our noise model. Finding good values for  $\beta$  that minimize  $\mathcal{L}_{4S}$  is difficult in practice, since the image rotation  $\phi_t$  must be taken into account during optimization. We tackle this problem by using the Python package PyTorch for gradient-based optimization (Paszke et al. 2019), leveraging its automatic gradient computation (Baydin et al. 2018). Gradients are calculated through sampler grids, initially developed for spatial transformer networks (Jaderberg et al. 2016), allowing effective back-propagation through the image rotations. We chose the L-BFGS optimizer (Liu & Nocedal 1989), which converged faster for our application than other optimizers such as SGD with momentum (Sutskever et al. 2013) or Adam (Kingma & Ba 2017). We also find that the use of mini-batches, as often used in neural networks, leads to significantly worse results. Therefore, the whole data set is used during each gradient step. This is likely due to noisy values of  $\bar{\mathbf{r}}$ , which contains the signal of the planet for each mini-batch. For large datasets that do not fit into GPU memory, gradient accumulation can be used.

### 4.3. Regularization

So far, the number of free model parameters of 4S is huge: Given a frame resolution of  $100 \times 100$  pixels,  $\mathbf{B}$  contains 100 million parameters. To mitigate the risk of

overfitting, we use two types of regularization to reduce the expressiveness of the model: First, a classical L2 penalty term on the model parameters (similar to ridge regression; see chapter 3.1.4 of Bishop 2006), which we add to the loss function:

$$\mathcal{L}_{4S} = \underbrace{\frac{1}{N} \sum_{t=1}^N \|\mathbf{r}_t - \bar{\mathbf{r}}\|^2}_{\text{temporal variance}} + \underbrace{\lambda \cdot \|\beta\|^2}_{\text{L2 penalty}}, \quad (13)$$

where  $\lambda$  is the only hyperparameter of 4S. Larger values of  $\lambda$  force the parameters  $\beta$  to be closer to zero, reducing the expressiveness of the model. This means that a smaller value of  $\lambda$  results in a stronger reduction of the speckle noise while coming at the risk of overfitting (i.e., memorizing the data). In contrast to PCA, we notice that the best choice of  $\lambda$  does not depend on the separation from the star. Instead, it depends on the temporal and spatial resolution of the science frames. If only a few frames are available in time, a stronger regularization (i.e., larger values of  $\lambda$ ) is needed and the reduction of speckle noise is less effective. However, a detailed analysis of how to tune  $\lambda$  is beyond the scope of this paper.

In addition to the L2 regularization, we also convolve the column vectors of  $\mathbf{B}$  with the unsaturated PSF:

$$\mathbf{B}_{[:,n_i j+i]} = (\beta_{(i,j)} \circ \mathbf{m}_{(i,j)}) \circledast \text{PSF}. \quad (14)$$

The convolution ties spatially adjacent parameters together, reducing the effective number of model parameters. From our domain knowledge, we know that speckles approximately follow the shape of the PSF. All features

in the data that are smaller are not due to the speckle noise, but are caused, for example, by detector noise. By convolving the parameters  $\beta$  with the PSF, we prevent our model from overfitting pixel level artifacts.

#### 4.4. Main steps of 4S

Applying 4S to ADI data in HCI consists of the following steps, which we illustrate in Figure 6:

- ① **Data preparation:** Similar to PCA, 4S works on normalized data. We first subtract the temporal mean  $\bar{\mathbf{x}}$  and divide by the standard deviation along the time axis:

$$\mathbf{x}_t = (\mathbf{x}_{t,\text{raw}} - \bar{\mathbf{x}}) / \text{std}(\mathbf{x}_{t,\text{raw}}) \quad (15)$$

The additional division by  $\text{std}(\mathbf{x}_{t,\text{raw}})$  is required to ensure that the L2 regularization affects all areas in the image equally. The 2D science frames are flattened into one-dimensional vectors and stacked into the data matrix  $\mathbf{X} \in \mathbb{R}^{N \times D}$  (cf. the PCA procedure in Section 2).

- ② **Optimization of model parameters:** We initialize all parameters  $\beta$  with zeros and create the *right reason* mask  $\mathbf{m}_{(i,j)}$  for all output pixel positions. Afterward, we optimize  $\beta$  to minimize the loss function in Equation (13) using an L-BFGS optimizer.
- ③ **Calculation of the residual:** After the optimization is completed, we calculate the residual sequence using Equation (4). As for PCA, the final residual is obtained by averaging along the time dimension (Equation (5)).

We note that the subtraction of the temporal average in step 1 is not free from planet self-subtraction. More advanced ideas to overcome this step should be explored in future work. Our Python implementation takes advantage of modern NVIDIA A100 and H100 GPUs to speed up the optimization. Depending on the spatial and temporal resolution of the dataset, the optimization converges in about 10 to 30 minutes using one GPU.

## 5. QUANTITATIVE ANALYSIS

Comparing the contrast performance of post-processing techniques can be difficult for two main reasons: First, different post-processing methods follow fundamentally different concepts. PCA and 4S are both subtraction-based techniques. They return a residual image, which is analyzed in a second step with statistical methods like t-tests or STIM maps (Mawet et al. 2014; Pairet et al. 2019). Methods like FMMF, PACO or TRAP (Ruffio et al. 2017; Flasseur et al. 2018; Samland et al. 2021) belong to the family of inverse problem approaches. They produce detection maps that show the models’ belief in the presence of a planet. The detection process for

subtraction-based and inverse-problem approaches rely on very different statistics. Therefore, their results are not directly comparable. In addition, the residual noise characteristics are method-specific and usually unknown. This makes a fair comparison even more difficult. Especially if we want to compare different methods given the same False Positive Fraction (FPF). For this reason, methods should only be compared within the same category (see, e.g., Cantalloube et al. 2021).

Secondly, the contrast performance is influenced by the instrument and the observing mode. Depending on the wavelength, different noise sources dominate, such that the best choice of post-processing method is likely to be instrument-dependent. To keep our analysis consistent, we decided to focus on archival data from the VLT-NACO instrument in the  $L'$ -band ( $\lambda = 3.8 \mu\text{m}$ ). The exposure times of these data are typically very short, which gives us a high temporal resolution. This is crucial for 4S to minimize the risk of overfitting. It also allows us to correct not only for quasi-static speckles, but also for atmospheric speckles on shorter time scales. To ensure the robustness of our results under changing observing conditions and targets, we base our analysis on 11 archival datasets (see Table 1). This guarantees that any observed improvements are not random, but consistent across multiple datasets. All targets are bright ( $L' < 4$  mag) and were chosen such that no obvious companions or disc signals are present. We ensure that each dataset has at least 30 minutes of observations in seeing conditions no worse than  $r_0 < 1.5$ . The final list is a random selection of datasets in the archive that satisfy these conditions.

We process all our datasets with the state-of-the-art pipeline PynPoint. The preprocessing steps include: 1. a simple dark and flat calibration, 2. an interpolation of bad pixels, 3. a simple background subtraction using sky frames, and 4. a centering of the star using cross-correlations. To keep the computation time manageable, we combine every 5 frames of the science sequence and crop the frames to a field of view of radius  $1.2''$  (equivalent to  $12 \lambda/D$ ). Even after temporal binning, we still have between 2400 and 13 000 frames along the time dimension. The final pre-processed data cubes are publicly available on Zenodo (Bonse 2024a).

### 5.1. Right for the right reasons

In Section 3.2, we used saliency maps to better understand which information is used by PCA to estimate the noise at a given position. This approach revealed that PCA converges to the telescope’s PSF for high numbers of components, causing significant signal loss. 4S is designed to overcome this limitation and forces the model to explore other explanations for the speckle noise using a *right reason constraint*. But is the noise estimate of 4S *right for the right reasons*?

**Table 1.** VLT-NACO datasets used for performance evaluation.

#	Target	Program ID	Observing date	$r_0$ (")	Field rotation ( $^\circ$ )	DIT (s)	total (s)	AGPM
1	HD 2262	199.C-0065 (C) <sup>a</sup>	2017-11-01	0.56	73.7	0.35	5043	✓
2	HD 7570	1101.C-0092 (C) <sup>c</sup>	2018-11-27	0.65	68.9	0.35	6895	✓
3	HD 11171	1101.C-0092 (C) <sup>c</sup>	2018-11-28	0.63	108.7	0.35	7350	✓
4	HD 22049	096.C-0679 (A) <sup>c</sup>	2015-12-17	0.57	90.1	0.08	4608	✓
5	HD 22049	199.C-0065 (C) <sup>a</sup>	2017-10-30	0.61	104.7	0.08	5304	✓
6	HD 38678	084.C-0396 (A) <sup>b</sup>	2009-11-27	1.47	39.2	0.2	2460	
7	HD 40136	1101.C-0092(C) <sup>c</sup>	2018-11-29	0.87	114.7	0.3	7500	✓
8	HD 115892	1101.C-0092 (E) <sup>c</sup>	2019-05-23	0.48	95.2	0.35	6895	✓
9	HD 169022	1101.C-0092 (E) <sup>c</sup>	2019-05-20	1.28	113.8	0.35	6195	✓
10	HD 177724	091.C-0654 (A) <sup>c</sup>	2013-08-19	0.65	24.9	0.2	3200	
11	HD 209952	089.C-0149 (A) <sup>b</sup>	2012-07-14	1.12	40.4	0.2	2880	
12	HD 35850	088.C-0085(A) <sup>b</sup>	2011-10-21	1.1	69.6	0.2	3120	

NOTE— Datasets #1 through #11 are used for the quantitative analysis; dataset #12 (AF Lep) is used for the scientific demonstration in Section 6. All datasets are pre-processed with `PynPoint` and publicly available on Zenodo (Bonse 2024a).

**References**— *a*: Launhardt et al. (2020), *b*: Rameau et al. (2013), *c*: no reference or unpublished

Similar to PCA, we can compute saliency maps for 4S which are just the column vectors of our noise model:

$$M_{(i,j)} = |\mathbf{B}|_{[:,n_i j+i]}. \quad (16)$$

We run 4S on the datasets #4 (HD 22049) and #7 (HD 40136) with a regularization strength  $\lambda = 10^3$  and compute saliency maps for three different positions. The two datasets were selected randomly, with about three years between observations. The output saliency maps are shown in Figure 7. We notice that 4S no longer learns the shape of the telescope’s PSF, but instead explores other areas in the science frames. The most dominant feature in the saliency maps of 4S are strong point symmetries. This is a strong indication that 4S indeed learns the characteristic behavior of speckles, which are known to exhibit symmetric or antisymmetric correlations (Bloemhof et al. 2001; Perrin et al. 2003; Bloemhof 2007; Ribak & Gladysz 2008). Another pattern, characterized by four points of equal distance from the star, can be seen in the lower left saliency map of Figure 7. This pattern is due to waffle mode, a distortion of the wavefront that is not visible to the wavefront sensor. It is an artifact in the data that we want to remove in the data post-processing. Due to the width of the  $L$ -band filter, the speckles are slightly elongated. 4S finds this characteristic of the speckle noise and uses information on a line pointing towards the center of the frame (bottom two frames of Figure 7).

The two datasets, #4 (HD 22049) and #7 (HD 40136), were acquired with the same observing mode. However, there is a significant gap of three years between the two observations. Despite this time difference, it is remarkable to observe the similarity in the saliency

maps produced by 4S. This suggests that 4S can learn signatures of the noise that are linked to the instrument and not the individual observation. This result opens up several possibilities for future work, which we discuss in Section 7.

## 5.2. Fake planet experiments

To reliably calculate the contrast performance of 4S, we perform extensive fake planet experiments. We use *contrast grids* implemented in the `python` package `applefy` (Bonse et al. 2023). Contrast grids systematically calculate the S/N of inserted fake companions as a function of distance from the star and planet brightness. We insert fake planets every 0.5 mag for contrasts [5, 15] mag, and for separations [1.5, 12.5]  $\lambda/D$  every  $0.5\lambda/D$ . For each combination of planet brightness and separation, three planets are inserted at different position angles. We insert only one fake planet at a time, resulting in 945 fake planet experiments per dataset. Each dataset with an inserted fake planet is processed with PCA and 4S to obtain a residual image. Afterward, the S/N of the companion is calculated using the method proposed by Mawet et al. (2014). Since our limits are in the speckle-dominated regime, we use spaced pixels instead of apertures to extract the photometry, as suggested by Bonse et al. (2023). The final contrast curves are obtained by thresholding the contrast grid using all 945 fake planet experiments.

The results of PCA depend strongly on the number of components used. Therefore, 33 different setups with  $K \in [1, 500]$  were calculated for each fake planet experiment. For 4S, the regularization strength was set to  $\lambda \in [10^2, 10^3, 10^4, 10^5]$ . We compute contrast grids for

### 4S Saliency Map

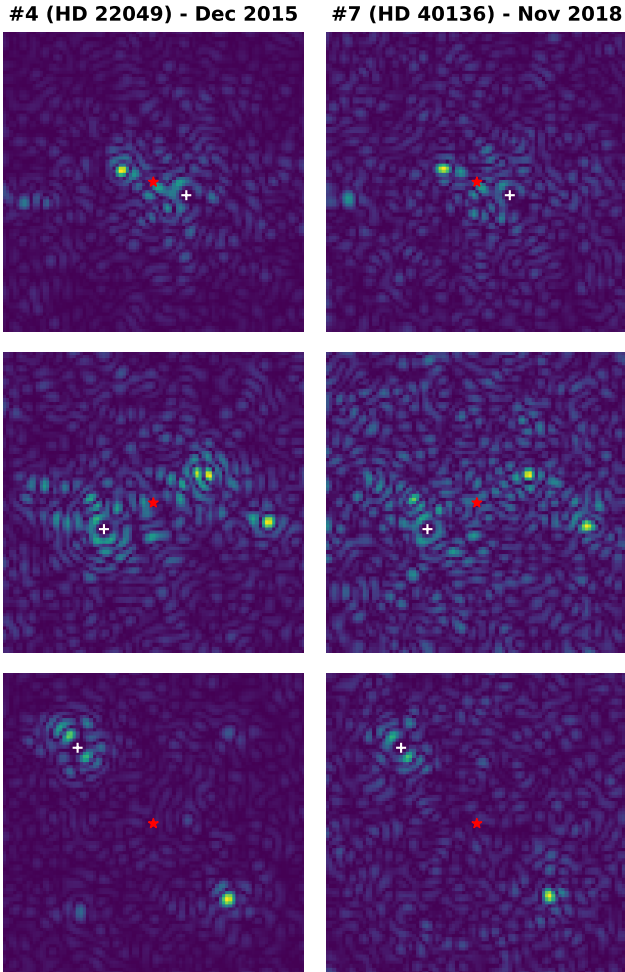


**Figure 7.** Saliency maps for 4S, computed for the datasets #4 (HD 22049) (left column) and #7 (HD 40136) (right column). The saliency maps show which information from the science frames  $\mathbf{x}_t$  is used by 4S to estimate the noise at the position marked by the white cross. In contrast to PCA (cf. Figure 3), 4S successfully learns the point-symmetric signatures of the speckle noise. The red star marks the center of the frame.

each dataset (see Table 1) and all algorithm setups. In total, we compute more than 300 000 PCA and more than 30 000 4S residuals. This experiment required substantial compute and was thus realized on a compute cluster, allowing us to use up to 200 NVIDIA A100 / H100 GPUs simultaneously. To further speed up the computations, we reimplemented the PynPoint version of PCA using PyTorch to enable GPU computations. Our new GPU implementation of PCA uses the fast SVD from Halko et al. (2011), resulting in a 50-fold speedup on one NVIDIA H100 GPU compared to 64 CPUs. The code for our new implementation is available along with our Python package `fours`. Example

residuals and contrast curves for one of our datasets #5 (HD 22049) are shown in Figure 8. As shown in the plot, 4S reaches significantly deeper contrast compared to PCA, especially at separations close to the star. The two close fake companions at  $1.5\lambda/D$  and  $2.5\lambda/D$  are undetectable with PCA, regardless of the number of principal components. For separations  $< 2.5\lambda/D$ , we reach about 1.4 mag deeper contrast with 4S compared to PCA. Even at larger separations, a decent improvement of about  $\sim 0.3$  mag can be achieved. Although 4S is designed to prevent planet self-subtraction, we still observe negative wings next to the planet’s signal at close separations. These negative wings are caused by the subtraction of the temporal average in the first step of 4S. If we were able to subtract the temporal mean without the planet signal, the negative wings would disappear and even better results could be achieved. This path should be explored in future work within the context of RDI.

To achieve the deepest contrast of PCA, we need to carefully tune the number of components for each separation. While 16 components give the best results at  $\sim 3\lambda/D$ , 400 components are required at  $\sim 12\lambda/D$ . For 4S, on the other hand,  $\lambda = 100$  consistently outperforms all PCA setups. Since tuning the number of principal components is difficult in practice and could suffer from human bias, this is a clear advantage of 4S.

We repeat the same experiment shown in Figure 8 for all datasets summarized in Table 1. Depending on the dataset, we select the best  $\lambda \in [10^2, 10^3, 10^4, 10^5]$  for 4S and compare it to the *optimal* PCA limits. For datasets #10 and #11 we had to exclude the result for the innermost  $2.5\lambda/D$  due to strong over-saturation from the host star. The relative improvement of 4S over PCA accumulated over all datasets is shown in Figure 9.

The results are consistent with the improvement achieved on dataset #5, with about 0.5 mag variation depending on the dataset. The improvement is largest at close separations to the star. We know that the loss of the planet signal in PCA is at its maximum at these separations (see Section 3). 4S successfully mitigates this limitation, allowing it to learn a better representation of the speckle noise.

The improvement of 4S over PCA is probably larger in practice, mainly for three reasons:

- If we go through the stack of PCA residuals for different numbers of components, the speckles pattern changes considerably. For 4S the speckle pattern in the residual images is very static for different values of  $\lambda$ . Since we try 33 different setups for PCA, the chance of a speckle co-aligning with the inserted fake companion increases. This artificially increases the S/N in the PCA residuals.
- It is likely that the *optimal* PCA limit is not reached in practice. This is because it is difficult to find the best number of principal components. For dataset #4 (HD 22049), Launhardt et al. (2020)

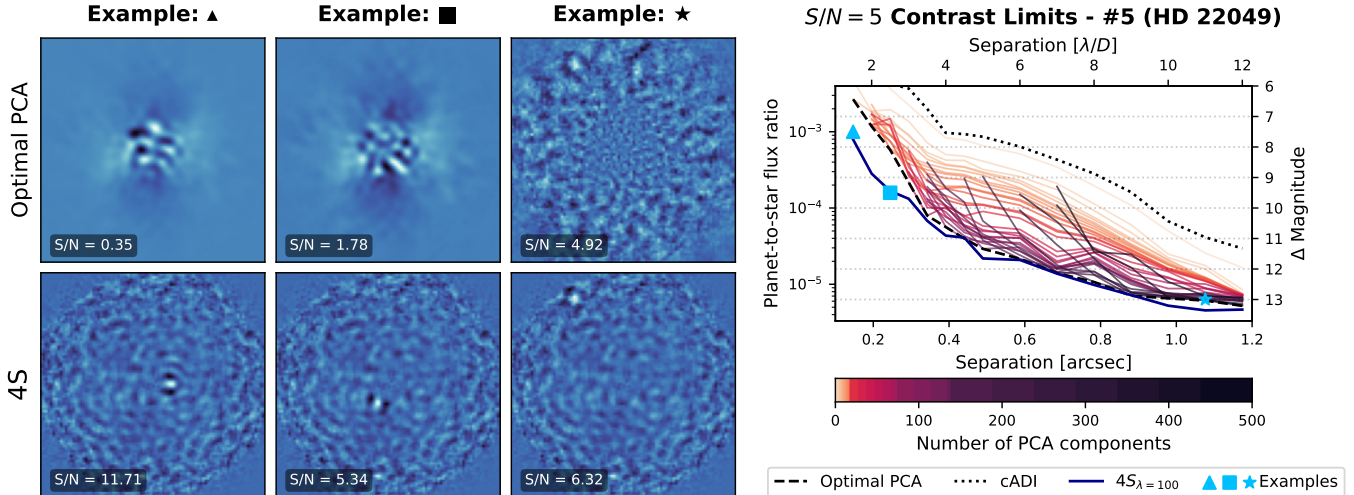


**Figure 8.** Results of our fake planet experiments for dataset #5 (HD 22049) (see Table 1). On the left, example residuals are shown for fake planets at  $\blacktriangle = (1.5 \lambda/D, 7.5 \text{ mag})$ ,  $\blacksquare = (2.5 \lambda/D, 9.5 \text{ mag})$  and  $\star = (11 \lambda/D, 13 \text{ mag})$ . In the case of PCA, we tune the number of principal components to get the deepest contrast (*optimal PCA*). For 4S, we use the same setup with  $\lambda = 100$  for all separations. An interactive version of the plot is available on our [documentation page](#). The plot on the right shows contrast curves of 4S and PCA with different numbers of principal components. Each contrast curve was obtained by computing a contrast grid using the Python package `applefy` and is based on 945 fake planet experiments. The dotted black line gives the cADI contrast, which is equivalent to a simple subtraction of the temporal median. Note that for large numbers of components and small separations, none of the inserted fake planets reaches a  $S/N > 5$ .

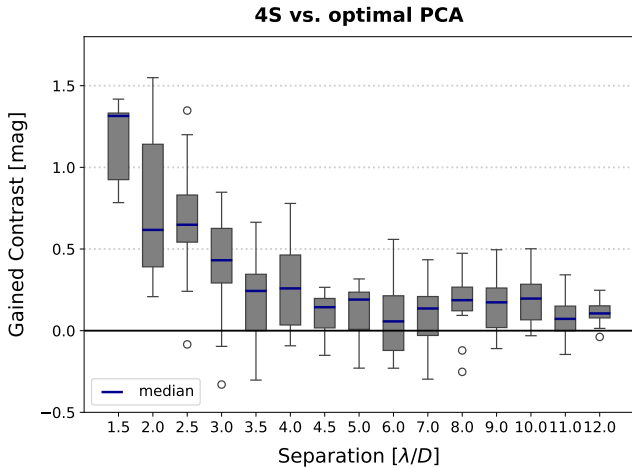


**Figure 9.** Relative improvement in contrast of 4S over PCA, accumulated over the 11 datasets shown in Table 1. The blue line shows the median improvement, the gray boxes give the interquartile range (IQR), and the whiskers extend to points that lie within 1.5 IQR. The points marked as circles are outliers.

report a contrast of 10.5 mag at  $0.5''$  and 11.6 mag at  $0.75''$ . Our *optimal PCA* limits reach down to 11.5 mag at  $0.5''$  and 12.3 mag at  $0.75''$ , which is almost one magnitude deeper. This difference is likely due to the large number of setups tried in our PCA analysis. In addition, better pre-processing

of the data with PynPoint could explain part of this improvement.

- The noise distribution of the PCA residuals often deviates from Gaussian noise (Pairet et al. 2019; Bonse et al. 2023). This is especially true for small numbers of principal components. Heavy tailed non-Gaussian residual noise increases the risk of false positives. In Appendix A, we study the residual noise distribution of 4S and PCA. We find that the noise of 4S is not perfectly Gaussian either, but it is more Gaussian than the residual noise of PCA. This means that the chance of observing a  $S/N > 5$  that is caused by noise is greater for PCA than for 4S. However, since the true noise distribution is unknown for both methods, the limits cannot be calculated at the same FPF level.

Over all datasets, the median contrast performance of 4S is consistently better than limits reached with *optimal PCA*. This improvement opens a new discovery space on archival data and for future observations.

## 6. SCIENTIFIC DEMONSTRATION

To demonstrate that 4S is not only capable of improving the contrast performance for artificial companions, we have searched the ESO archive for companions that have been found with VLT-SPHERE but not with VLT-NACO. VLT-SPHERE has found several new companions, but unfortunately most of them have never been observed with VLT-NACO.

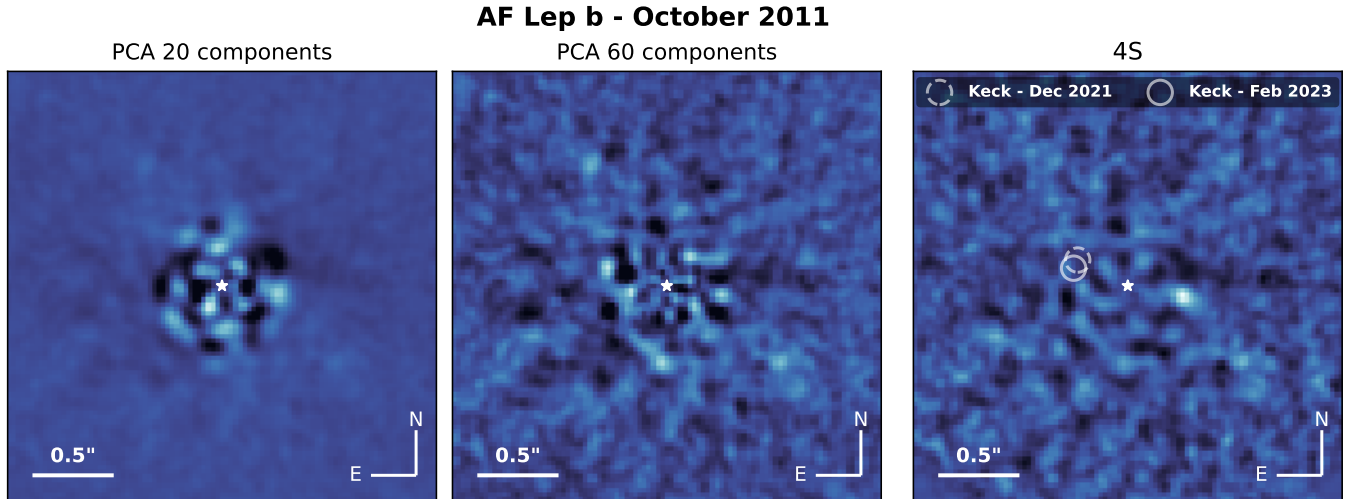


**Figure 10.** Residual images of the AF Lep dataset (#12 in Table 1) taken with VLT-NACO in 2011. The two images on the left show the residuals obtained with PCA with  $K = 20$  and  $K = 60$  components, respectively. The image on the right shows the residual of 4S, which reveals the giant exoplanet AF Lep b at  $S/N = 6.8$ , 11 years before its discovery. For better visibility, we filter the residual images with a Gaussian kernel ( $\sigma = 0.8$  pixel). The  $S/N$  is calculated on the raw residuals before applying the Gaussian filter. An interactive version of the plot for different setups of PCA and 4S is available in our [online documentation](#). A gallery of all PCA and 4S residuals is given in Figure 15.

AF Leporis is a young ( $\sim 28$  Myr based on moving group age estimate, Bell et al. 2015) F8V-type star (Gray et al. 2006) belonging to the  $\beta$  Pictoris moving group (Zúñiga-Fernández et al. 2021). Since AF Lep presents a significant astrometric HIPPARCOS - GAIA acceleration, it was observed by multiple direct imaging surveys targeted at accelerating stars. Three direct detections of the companion AF Lep b obtained with VLT-SPHERE and Keck-NICR2 were claimed almost simultaneously in 2023 (De Rosa et al. 2023; Mesa et al. 2023; Franson et al. 2023). While these observations firmly place AF Lep b as a faint L-type dwarf in the planetary regime, estimations of its dynamical mass via the astrometric acceleration are conflicting between instruments and with age-luminosity model-based estimates. While the latter disagreement is often observed in recent analyses (Cheetham et al. 2018; Brandt et al. 2021a; Tobin et al. 2024), the former is likely due to the very short time-baseline on which the orbit of AF Lep b could be sampled (December 2021 to February 2023; see Figure 11).

Franson et al. (2023) discovered the planet in the  $L'$ -band at a separation of  $\rho_{2023.090342} = 342 \pm 8$  mas and at a contrast of  $\Delta L' = 9.94 \pm 0.14$  mag. This is precisely the regime where we expect an improvement with 4S over PCA. The star AF Lep was imaged with VLT-NACO in 2011 at  $L'$ -band using the normal imaging mode (see Table 1). The dataset was taken in medium observing conditions (seeing  $1.1''$ ), but provides  $69.6^\circ$  of field rotation. We process this archival dataset with PynPoint (Stolker et al. 2019) using the same preprocessing routine explained in Section 5, and then subtract the stellar PSF using PCA and 4S. Our 4S reduction reveals the giant

exoplanet AF Lep b on the opposite side of the star, 11 years before its discovery in 2022 (see Figure 10). The signal of the planet is also present in the residuals of PCA, but it is indistinguishable from the speckle noise.

This preccovery of AF Lep b presents a unique opportunity to extend the time-baseline of its orbit sampling from about 1 yr to more than 11 yr. Furthermore, it enables an independent confirmation of the existing  $L'$ -band magnitude estimate (Franson et al. 2023).

*Astrometry and Photometry*—Because of the attenuation of the planet signal due to the post-processing, we cannot extract the photometry and astrometry from the residual images directly. In the case of PCA, it is common practice to insert a negative fake planet into the raw data at the position of the detection. The photometry and astrometry, as well as their uncertainties, are then calculated using MCMC (see, e.g., Stolker et al. 2019). Each step in the MCMC requires a complete recalculation of the PCA basis and the residual. A full MCMC often relies on several thousand re-reductions, which becomes computationally expensive. For 4S, a reduction of the AF Lep dataset takes about 10 minutes, resulting in a total computation time of about one month. It is likely possible to significantly reduce the computation time required for an MCMC with 4S. This could be achieved by avoiding the recalculation of the projection matrix  $\mathbf{B}$  for each iteration. Instead,  $\mathbf{B}$  could be calculated once and then updated continuously during the MCMC optimization. However, to verify the accuracy of such an approach, further tests are needed that are beyond the scope of this paper. Further details for future work in this direction are discussed in Section 7. Instead, we decided to estimate the astrom-

**Table 2.** Properties of AF Lep b.

$\rho_{2011.800}$ (mas)	$323.24^{+6.71}_{-6.44}$
$\theta_{2011.800}$ ( $^{\circ}$ )	$258.81^{+0.53}_{-0.59}$
$\Delta L'$ (mag)	$10.03^{+0.13}_{-0.12}$
$L'$ (mag)	$14.96^{+0.14}_{-0.13}$
$M_{L'}$ (mag)	$12.81^{+0.14}_{-0.13}$
Primary mass ( $M_{\odot}$ )	$1.219^{+0.052}_{-0.054}$
Secondary mass ( $M_J$ )	$3.74^{+0.53}_{-0.50}$
Semi-major axis (au)	$9.01^{+0.20}_{-0.19}$
Inclination ( $^{\circ}$ )	$55.8^{+6.2}_{-7.2}$
Ascending node ( $^{\circ}$ )	$69.7^{+5.6}_{-5.4}$
Mean longitude at 2010.0 ( $^{\circ}$ )	$170^{+11}_{-13}$
Eccentricity	$0.031^{+0.027}_{-0.020}$
Argument of periastron ( $^{\circ}$ )	$-10^{+66}_{-52}$

NOTE— Reported uncertainties are the median with the 16 % and 84 % quantiles of the MCMC samples after burn-in.

etry and photometry based on the PCA residuals using the well-established and tested MCMC code presented in [Stolker et al. \(2019\)](#). For this, we first calculated PCA residuals for  $K \in [1, 200]$  every 10 components. The peak S/N = 4.7 is reached at 65 components. We fix  $K = 65$  and use the MCMC procedure in `PynPoint` to estimate the astrometry and photometry. As in [Stolker et al. \(2019\)](#), we first use a simplex minimization to find good initialization parameters. Afterward, we run the MCMC for 500 steps using 100 walkers. Our results are summarized in Table 2. The estimated photometry of  $\Delta L' = 10.03^{+0.13}_{-0.12}$  mag is in perfect agreement (i.e., within one standard deviation) with the results of [Franson et al. \(2023\)](#), who reported  $\Delta L' = 9.94 \pm 0.14$  mag.

*Orbit Fit*—We combine the new relative astrometry data point obtained in this work with the relative astrometry points from the three AF Lep b detection papers ([De Rosa et al. 2023](#); [Mesa et al. 2023](#); [Franson et al. 2023](#)), HIPPARCOS (see [van Leeuwen 2007](#)) and GAIA ([Prusti et al. 2016](#); [Vallenari et al. 2023](#)) acceleration as well as archival RV data published by [Butler et al. \(2017\)](#). To combine the data into a single orbit fit, we use the MCMC-based orbit fitting package `orvara` ([Brandt et al. 2021b](#)). We fit for all orbital parameters and the primary and secondary mass, setting the default priors as defined in Table 4 of [Brandt et al. \(2021b\)](#). To stay comparable to the results in [Franson et al. \(2023\)](#), we also set a highly constrained Gaussian prior on the mass of AF Lep:  $M = 1.20 \pm 0.06 M_{\odot}$  ([Kervella et al. 2022](#)). We run the Monte Carlo chain to 500 000 samples over 100 walkers, discarding the first 20 % of each chain as burn-in. The parameter distributions and resulting fit values are reported in Figure 11 and Table 2. We report a dynamical mass estimate of  $M = 3.74^{+0.53}_{-0.50} M_J$ , con-

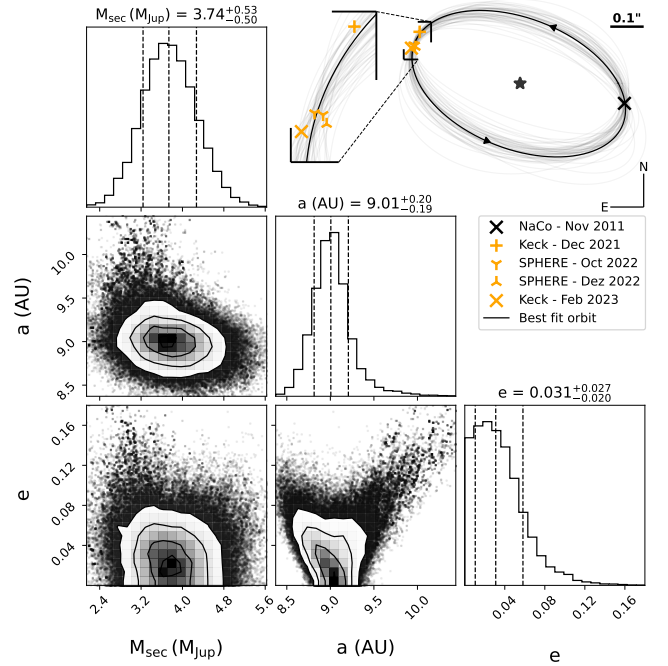


**Figure 11.** Results from the updated orbit fit of AF Lep b. The corner diagram reports the posterior distribution of an MCMC-based orbit fit using `orvara`. The median with the 16 % and 84 % quantiles is reported. The top-right inset shows all available relative astrometry measurements with the best orbital fit. To illustrate the confidence of the fit, 100 orbits are drawn from the fit posterior (gray). For a summary of all results, see Table 2.

firming its status well within the planetary-mass regime. This estimate offers a significant improvement over and is compatible with the masses reported in [Franson et al. \(2023\)](#) and [De Rosa et al. \(2023\)](#).

As the additional VLT-NACO data point is almost precisely opposite to the more recent observations, it offers an ideal opportunity to constrain the orbit’s eccentricity. Indeed, we find AF Lep b to move on a circular orbit ( $\epsilon = 0.031^{+0.027}_{-0.020}$ ). Considering that due to the low mass of the companion it likely formed in-situ in the protoplanetary disk, our measurement agrees much better with tentative evidence of planet-mass companions occurring preferentially on circular orbit ([Bowler et al. 2020](#)). We note, that due to the relative astrometry point being opposite, we do not improve the fit of the inclination. This circular orbit agrees with recent interferometric observations of the planet with VLTI-GRAVITY ([Balmer et al. subm.](#)).

In addition to the 2011 observation, AF Lep was observed a second time with VLT-NACO in 2015 (prog. ID 096.C-0679(A); [Launhardt et al. 2020](#)). Our re-analysis of this dataset did not yield a detection. In 2015, the projected separation of the planet from the star is much smaller ( $\lesssim 2 \lambda/D$ ) than in 2011, resulting in higher con-



trast requirements. Therefore, the non-detection in 2015 is consistent with our contrast limits and orbit fit.

## 7. FUTURE WORK

The detection of AF Lep b in archival VLT-NACO data demonstrates the potential of 4S to find previously missed companions. The archive of VLT-NACO observations comprises more than 800 datasets from more than 450 stars (considering only  $L'$ -band data taken in pupil tracking mode). It is possible that a re-analysis of these datasets will reveal additional companions. Future work should consider a re-analysis not only for VLT-NACO data, but also for other instruments. In this way, a better understanding of the contrast performance of 4S for different observing modes and instruments can be obtained. The use of saliency maps together with 4S may help us to better understand the optics and speckle pattern. If some difficult-to-interpret patterns are systematically visible in the saliency maps of an instrument, they may indicate overlooked effects in the instrument optics. This could open the door to new developments on the hardware side.

The primary drawback of 4S is its computational cost. Processing one dataset takes about 10–30 minutes on a single NVIDIA A100/H100 GPU. While this computation time is unproblematic for detection purposes, it quickly becomes infeasible for scientific analysis. Extracting astrometry and photometry, or calculating detection limits, requires re-processing the same dataset hundreds of times. In fact, the most computationally expensive step in 4S is the optimization of the projection matrix in step 2 (see Figure 6). We recompute the projection matrix from scratch for all our fake planet experiments. This might not be necessary. Future work should explore strategies to compute the matrix once and update it as the scientific analysis progresses. Fast GPU-based MCMC implementations compatible with our code are available, for example, in `pyro` (Bingham et al. 2019). The L-BFGS optimizer used in this work requires a lot of GPU memory, especially for large science frames. This sets the maximum resolution which can still be processed with one NVIDIA A100/H100 GPU to about  $150 \times 150$  pixels, depending on the temporal resolution of the dataset. We recommend cropping the science frames to benefit from the better contrast performance of 4S at close separations. Unfortunately, this memory requirement currently prevents us from processing the datasets of the exoplanet imaging data challenge (Cantalloube et al. 2015). Future work should focus on making our implementation more memory efficient, for example, by using gradient accumulation during optimization.

*Further development of the method*—The noise model of 4S is a simple linear model. Especially at separations close to the star and in data taken with a coronagraph, non-linear artifacts can occur. For this purpose, the linear model of 4S in Equation (10) could be replaced

by a neural network. Neural networks have already been proposed for speckle subtraction in HCI (see Wolf et al. 2023). In Section 5, we observed that a substantial part of the information used by 4S to explain the speckle noise are symmetries across the entire frame. Therefore, neural networks should not be used locally as in Wolf et al. (2023), but globally. A possible direction for this could be masked auto-encoders (He et al. 2022).

A number of new post-processing methods based on PCA have been proposed in the literature. One example is the RSM map of Dahlqvist et al. (2020), which replaces the last step in PCA, the averaging along time and allows combining multiple post-processing algorithms. Another example is the combination of PCA with forward modeling (FMMF; Ruffio et al. 2017). The basic steps of 4S are identical to those of PCA, which is why methods such as RSM and FMMF can also be used with 4S. For this reason, 4S should be seen as a building block for new post-processing methods.

Our analysis of the saliency maps in Section 5 has shown that the noise model learned by 4S hardly changes over years. This is a strong indicator that 4S could also be used with RDI. For RDI, the noise model of 4S needs to be learned only once and can then be applied to many datasets. This procedure also avoids the high computational costs of 4S for ADI. The parameters of 4S could be conditioned on observation conditions, as suggested by Gebhard et al. (2022) for half-sibling regression. In combination with RDI, we might be able to obtain a universal model of the speckle noise that utilizes all previously collected data.

## 8. SUMMARY & CONCLUSIONS

In this paper, we have gained a deep understanding for the loss of planet signal in PCA-based post-processing. Using saliency maps, we identified two main reasons for this loss: first, the convergence of the PCA noise model to the telescope PSF; and second, a problematic loss function that misleads the noise estimate to fit the planet signal. Building upon these insights, we developed a new post-processing algorithm that overcomes the limitations of PCA. We named this method 4S (Signal Safe Speckle Subtraction). 4S is characterized by three innovations: First, a linear noise model with a right reason constraint, second, a new loss function that is invariant to the planet signal, and third, a domain knowledge-informed regularization.

We applied 4S to archival data from the VLT-NACO instrument to compare its contrast performance to PCA. On a sample of 11 datasets, we observed a contrast improvement of up to 1.5 magnitudes, especially at close separations to the star. In addition to achieving deeper contrast, 4S produces residual noise that is more Gaussian compared to PCA (see Appendix A), reducing the risk of false positives. The main reason for this improvement is the ability of 4S to learn a better representation of the speckle noise. A detailed analysis revealed that 4S

can recover speckle pattern that we would expect from the theory. The increase in contrast performance allowed us to detect the giant exoplanet AF Lep b in archival data from 2011, 11 years before its discovery. Using this new astrometric point, we significantly improve the constraints on the orbital parameters of the planet.

The introduction of 4S marks a leap for the post-processing of high-contrast imaging (HCI) data. Looking ahead, our findings have the potential to boost exoplanet detection on archival data and for future observations. We believe that the findings from our work will provide inspiration for the development of new post-processing methods beyond 4S.

## 9. ACKNOWLEDGMENTS

This work was supported by an ETH Zurich Research Grant. M.J.B. and S.P.Q. gratefully acknowledge the financial support from ETH Zurich. Parts of this work has been carried out within the framework of the National Centre of Competence in Research PlanetS supported by the Swiss National Science Foundation (SNSF). J.H. acknowledges the financial support from the Swiss National Science Foundation (SNSF) under project grant number 200020\_200399.

**Author contributions:** M.J.B. carried out the main analyses, developed the 4S algorithm and wrote the manuscript. He programmed the publicly available python package `fours` and wrote the documentation page. T.D.G. helped with the analysis and the development of 4S. His previous work on half-sibling regression algorithm has set the basis for this paper. F.A.D. carried out the orbit fits of AF Lep b and helped writing the corresponding section. S.P.Q. and B.S. provided access to the compute resources needed for this project. All authors discussed the algorithm, analysis and results. All authors commented on the manuscript.

**Used software:** This work has made use of a number of open-source Python packages, including `astropy` (The Astropy Collaboration et al. 2013, 2018, 2022), `matplotlib` (Hunter 2007), `numpy` (Harris et al. 2020), `pandas` (McKinney 2010), `photutils` (Bradley et al. 2024), `scikit-image` (van der Walt et al. 2014), `scikit-learn` (Pedregosa et al. 2011), `scipy` (Virtanen et al. 2020), `seaborn` (Waskom 2021), `torch` (Paszke et al. 2019), and `tqdm` (da Costa-Luis 2019).

## REFERENCES

- Absil, O., Milli, J., Mawet, D., et al. 2013, *Astronomy & Astrophysics*, 559, L12, doi: [10.1051/0004-6361/201322748](https://doi.org/10.1051/0004-6361/201322748)
- Ali, S., Abuhmed, T., El-Sappagh, S., et al. 2023, *Information Fusion*, 99, 101805, doi: [10.1016/j.inffus.2023.101805](https://doi.org/10.1016/j.inffus.2023.101805)
- Amara, A., & Quanz, S. P. 2012, *Monthly Notices of the Royal Astronomical Society*, 427, 948, doi: [10.1111/j.1365-2966.2012.21918.x](https://doi.org/10.1111/j.1365-2966.2012.21918.x)
- Arcidiacono, C., & Simoncini, V. 2018, in *Adaptive Optics Systems VI*, Vol. 10703 (International Society for Optics and Photonics), 1070331
- Balmer, W., et al. *subm.*
- Baydin, A. G., Pearlmutter, B. A., Radul, A. A., & Siskind, J. M. 2018, *Journal of Machine Learning Research*, 18, 1
- Bell, C. P. M., Mamajek, E. E., & Naylor, T. 2015, *Monthly Notices of the Royal Astronomical Society*, 454, 593, doi: [10.1093/mnras/stv1981](https://doi.org/10.1093/mnras/stv1981)
- Beuzit, J. L., Vigan, A., Mouillet, D., et al. 2019, *Astronomy and Astrophysics*, 631, A155, doi: [10.1051/0004-6361/201935251](https://doi.org/10.1051/0004-6361/201935251)
- Bingham, E., Chen, J. P., Jankowiak, M., et al. 2019, *Journal of Machine Learning Research*, 20, 1
- Bishop, C. M. 2006, *Pattern Recognition and Machine Learning*, Information Science and Statistics (New York: Springer)
- Bloemhof, E. E. 2007, *Optics Express*, 15, 4705, doi: [10.1364/OE.15.004705](https://doi.org/10.1364/OE.15.004705)
- Bloemhof, E. E., Dekany, R. G., Troy, M., & Oppenheimer, B. R. 2001, *The Astrophysical Journal*, 558, L71, doi: [10.1086/323494](https://doi.org/10.1086/323494)
- Bonse, M. J. 2024a, Raw data for: Use the 4S (Signal-Safe Speckle Subtraction), 0.1, Zenodo, doi: [10.5281/zenodo.11456704](https://doi.org/10.5281/zenodo.11456704)
- . 2024b, Intermediate results for: Use the 4S (Signal-Safe Speckle Subtraction), 0.1, Zenodo, doi: [10.5281/zenodo.11457071](https://doi.org/10.5281/zenodo.11457071)
- Bonse, M. J., Quanz, S. P., & Amara, A. 2018, *Wavelet Based Speckle Suppression for Exoplanet Imaging - Application of a de-Noiseing Technique in the Time Domain*, doi: [10.48550/arXiv.1804.05063](https://doi.org/10.48550/arXiv.1804.05063)
- Bonse, M. J., Garvin, E. O., Gebhard, T. D., et al. 2023, *The Astronomical Journal*, 166, 71, doi: [10.3847/1538-3881/acc93c](https://doi.org/10.3847/1538-3881/acc93c)
- Bowler, B. P., Blunt, S. C., & Nielsen, E. L. 2020, *The Astronomical Journal*, 159, 63, doi: [10.3847/1538-3881/ab5b11](https://doi.org/10.3847/1538-3881/ab5b11)
- Bradley, L., Sipőcz, B., Robitaille, T., et al. 2024, `astropy/photutils`: 1.12.0, Zenodo, doi: [10.5281/zenodo.10967176](https://doi.org/10.5281/zenodo.10967176)

- Brandt, G. M., Dupuy, T. J., Li, Y., et al. 2021a, *The Astronomical Journal*, 162, 301, doi: [10.3847/1538-3881/ac273e](https://doi.org/10.3847/1538-3881/ac273e)
- Brandt, T. D., Dupuy, T. J., Li, Y., et al. 2021b, *The Astronomical Journal*, 162, 186, doi: [10.3847/1538-3881/ac042e](https://doi.org/10.3847/1538-3881/ac042e)
- Butler, R. P., Vogt, S. S., Laughlin, G., et al. 2017, *The Astronomical Journal*, 153, 208, doi: [10.3847/1538-3881/aa66ca](https://doi.org/10.3847/1538-3881/aa66ca)
- Cantalloube, F., Mouillet, D., Mugnier, L. M., et al. 2015, *Astronomy & Astrophysics*, 582, A89, doi: [10.1051/0004-6361/201425571](https://doi.org/10.1051/0004-6361/201425571)
- Cantalloube, F., Gomez-Gonzalez, C., Absil, O., et al. 2021, arXiv:2101.05080 [astro-ph], doi: [10.1117/12.2574803](https://doi.org/10.1117/12.2574803)
- Cantero, C., Absil, O., Dahlgqvist, C. H., & Van Droogenbroeck, M. 2023, *Astronomy and Astrophysics*, 680, A86, doi: [10.1051/0004-6361/202346085](https://doi.org/10.1051/0004-6361/202346085)
- Chauvin, G., Desidera, S., Lagrange, A. M., et al. 2017, *Astronomy and Astrophysics*, 605, L9, doi: [10.1051/0004-6361/201731152](https://doi.org/10.1051/0004-6361/201731152)
- Cheetham, A., Ségransan, D., Peretti, S., et al. 2018, *Astronomy & Astrophysics*, 614, A16, doi: [10.1051/0004-6361/201630136](https://doi.org/10.1051/0004-6361/201630136)
- Christiaens, V., Gonzalez, C. A. G., Farkas, R., et al. 2023, *Journal of Open Source Software*, 8, 4774, doi: [10.21105/joss.04774](https://doi.org/10.21105/joss.04774)
- Cugno, G., Pearce, T. D., Launhardt, R., et al. 2023, *Astronomy & Astrophysics*, 669, A145, doi: [10.1051/0004-6361/202244891](https://doi.org/10.1051/0004-6361/202244891)
- Currie, T., Biller, B., Lagrange, A.-M., et al. 2023, *Direct Imaging and Spectroscopy of Extrasolar Planets*, arXiv. <http://ascl.net/2205.05696>
- da Costa-Luis, C. O. 2019, *JOSS*, 4, 1277, doi: [10.21105/joss.01277](https://doi.org/10.21105/joss.01277)
- Daglayan, H., Vary, S., Leplat, V., Gillis, N., & Absil, P.-A. 2023, *Direct Exoplanet Detection Using L1 Norm Low-Rank Approximation*, arXiv. <http://ascl.net/2304.03619>
- Dahlgqvist, C.-H., & Absil, O. 2021, *Astronomy & Astrophysics*, 646, A49, doi: [10.1051/0004-6361/202039597](https://doi.org/10.1051/0004-6361/202039597)
- Dahlgqvist, C.-H., Cantalloube, F., & Absil, O. 2020, *Astronomy & Astrophysics*, 633, A95, doi: [10.1051/0004-6361/201936421](https://doi.org/10.1051/0004-6361/201936421)
- De Rosa, R. J., Nielsen, E. L., Wahhaj, Z., et al. 2023, *Astronomy and Astrophysics*, 672, A94, doi: [10.1051/0004-6361/202345877](https://doi.org/10.1051/0004-6361/202345877)
- Flasseur, O., Bodrito, T., Mairal, J., et al. 2024, *Monthly Notices of the Royal Astronomical Society*, 527, 1534, doi: [10.1093/mnras/stad3143](https://doi.org/10.1093/mnras/stad3143)
- Flasseur, O., Denis, L., Thiébaud, É., & Langlois, M. 2018, *Astronomy & Astrophysics*, 618, A138, doi: [10.1051/0004-6361/201832745](https://doi.org/10.1051/0004-6361/201832745)
- Franson, K., Bowler, B. P., Zhou, Y., et al. 2023, *The Astrophysical Journal*, 950, L19, doi: [10.3847/2041-8213/acd6f6](https://doi.org/10.3847/2041-8213/acd6f6)
- Fulton, B. J., Rosenthal, L. J., Hirsch, L. A., et al. 2021, *The Astrophysical Journal Supplement Series*, 255, 14, doi: [10.3847/1538-4365/abfcc1](https://doi.org/10.3847/1538-4365/abfcc1)
- Gebhard, T. D., Bonse, M. J., Quanz, S. P., & Schölkopf, B. 2022, *Astronomy & Astrophysics*, 666, A9, doi: [10.1051/0004-6361/202142529](https://doi.org/10.1051/0004-6361/202142529)
- Gomez Gonzalez, C. A., Absil, O., Absil, P.-A., et al. 2016, *Astronomy & Astrophysics*, 589, A54, doi: [10.1051/0004-6361/201527387](https://doi.org/10.1051/0004-6361/201527387)
- Gomez Gonzalez, C. A., Absil, O., & Van Droogenbroeck, M. 2018, *Astronomy & Astrophysics*, 613, A71, doi: [10.1051/0004-6361/201731961](https://doi.org/10.1051/0004-6361/201731961)
- Gomez Gonzalez, C. A., Wertz, O., Absil, O., et al. 2017, *The Astronomical Journal*, 154, 7, doi: [10.3847/1538-3881/aa73d7](https://doi.org/10.3847/1538-3881/aa73d7)
- Gray, R. O., Corbally, C. J., Garrison, R. F., et al. 2006, *The Astronomical Journal*, 132, 161, doi: [10.1086/504637](https://doi.org/10.1086/504637)
- Halko, N., Martinsson, P. G., & Tropp, J. A. 2011, *SIAM Review*, 53, 217, doi: [10.1137/090771806](https://doi.org/10.1137/090771806)
- Harris, C. R., Millman, K. J., van der Walt, S. J., et al. 2020, *Nature*, 585, 357, doi: [10.1038/s41586-020-2649-2](https://doi.org/10.1038/s41586-020-2649-2)
- He, K., Chen, X., Xie, S., et al. 2022, in *2022 IEEE/CVF Conference on Computer Vision and Pattern Recognition (CVPR)* (New Orleans, LA, USA: IEEE), 15979–15988, doi: [10.1109/CVPR52688.2022.01553](https://doi.org/10.1109/CVPR52688.2022.01553)
- Hunter, J. D. 2007, *Computing in Science & Engineering*, 9, 90, doi: [10.1109/mcse.2007.55](https://doi.org/10.1109/mcse.2007.55)
- Jaderberg, M., Simonyan, K., Zisserman, A., & Kavukcuoglu, K. 2016, *Spatial Transformer Networks*, arXiv, doi: [10.48550/arXiv.1506.02025](https://doi.org/10.48550/arXiv.1506.02025)
- Janson, M., Squicciarini, V., Delorme, P., et al. 2021, *Astronomy and Astrophysics*, 646, A164, doi: [10.1051/0004-6361/202039683](https://doi.org/10.1051/0004-6361/202039683)
- Jensen-Clem, R., Mawet, D., Gomez Gonzalez, C. A., et al. 2017, *The Astronomical Journal*, 155, 19, doi: [10.3847/1538-3881/aa97e4](https://doi.org/10.3847/1538-3881/aa97e4)
- Jovanovic, N., Martinache, F., Guyon, O., et al. 2015, *Publications of the Astronomical Society of the Pacific*, 127, 890, doi: [10.1086/682989](https://doi.org/10.1086/682989)
- Kenworthy, M. A., Codona, J. L., Hinz, P. M., et al. 2007, *The Astrophysical Journal*, 660, 762, doi: [10.1086/513596](https://doi.org/10.1086/513596)
- Kervella, P., Arenou, F., & Thévenin, F. 2022, *Astronomy & Astrophysics*, 657, A7, doi: [10.1051/0004-6361/202142146](https://doi.org/10.1051/0004-6361/202142146)

- Kingma, D. P., & Ba, J. 2017, Adam: A Method for Stochastic Optimization, arXiv, doi: [10.48550/arXiv.1412.6980](https://doi.org/10.48550/arXiv.1412.6980)
- Kuhn, J. R., Potter, D., & Parise, B. 2001, The Astrophysical Journal, 553, L189, doi: [10.1086/320686](https://doi.org/10.1086/320686)
- Lafrenière, D., Marois, C., Doyon, R., Nadeau, D., & Artigau, É. 2007, The Astrophysical Journal, 660, 770, doi: [10.1086/513180](https://doi.org/10.1086/513180)
- Lagrange, A. M., Philipot, F., Rubini, P., et al. 2023, Astronomy and Astrophysics, 677, A71, doi: [10.1051/0004-6361/202346165](https://doi.org/10.1051/0004-6361/202346165)
- Langlois, M., Gratton, R., Lagrange, A.-M., et al. 2021, arXiv:2103.03976 [astro-ph]. <http://ascl.net/2103.03976>
- Launhardt, R., Henning, Th., Quirrenbach, A., et al. 2020, Astronomy & Astrophysics, 635, A162, doi: [10.1051/0004-6361/201937000](https://doi.org/10.1051/0004-6361/201937000)
- Lewis, B., Fitzgerald, M. P., Dodkins, R. H., Davis, K. K., & Lin, J. 2023, The Astronomical Journal, 165, 59, doi: [10.3847/1538-3881/aca761](https://doi.org/10.3847/1538-3881/aca761)
- Liu, D. C., & Nocedal, J. 1989, Mathematical Programming, 45, 503, doi: [10.1007/BF01589116](https://doi.org/10.1007/BF01589116)
- Macintosh, B., Graham, J. R., Ingraham, P., et al. 2014, Proceedings of the National Academy of Science, 111, 12661, doi: [10.1073/pnas.1304215111](https://doi.org/10.1073/pnas.1304215111)
- Macintosh, B., Graham, J. R., Barman, T., et al. 2015, Science, 350, 64, doi: [10.1126/science.aac5891](https://doi.org/10.1126/science.aac5891)
- Males, J. R., Fitzgerald, M. P., Belikov, R., & Guyon, O. 2021, arXiv:2107.04604 [astro-ph]. <http://ascl.net/2107.04604>
- Males, J. R., Close, L. M., Miller, K., et al. 2018, in Adaptive Optics Systems VI, Vol. 10703 (SPIE), 76–89, doi: [10.1117/12.2312992](https://doi.org/10.1117/12.2312992)
- Marois, C., Correia, C., Galicher, R., et al. 2014, in Adaptive Optics Systems IV, Vol. 9148 (International Society for Optics and Photonics), 91480U
- Marois, C., Lafreniere, D., Doyon, R., Macintosh, B., & Nadeau, D. 2006, The Astrophysical Journal, 641, 556, doi: [10.1086/500401](https://doi.org/10.1086/500401)
- Mawet, D., Serabyn, E., Liewer, K., et al. 2009, The Astrophysical Journal, 709, 53, doi: [10.1088/0004-637X/709/1/53](https://doi.org/10.1088/0004-637X/709/1/53)
- Mawet, D., Absil, O., Montagnier, G., et al. 2012, Astronomy & Astrophysics, 544, A131, doi: [10.1051/0004-6361/201219662](https://doi.org/10.1051/0004-6361/201219662)
- Mawet, D., Absil, O., Delacroix, C., et al. 2013, Astronomy & Astrophysics, 552, L13, doi: [10.1051/0004-6361/201321315](https://doi.org/10.1051/0004-6361/201321315)
- Mawet, D., Milli, J., Wahhaj, Z., et al. 2014, The Astrophysical Journal, 792, 97, doi: [10.1088/0004-637X/792/2/97](https://doi.org/10.1088/0004-637X/792/2/97)
- McKinney, W. 2010, in Proceedings of the 9th Python in Science Conference, ed. S. van der Walt & J. Millman, 56–61, doi: [10.25080/Majora-92bf1922-00a](https://doi.org/10.25080/Majora-92bf1922-00a)
- Mesa, D., Gratton, R., Kervella, P., et al. 2023, Astronomy and Astrophysics, 672, A93, doi: [10.1051/0004-6361/202345865](https://doi.org/10.1051/0004-6361/202345865)
- Meshkat, T., Kenworthy, M. A., Quanz, S. P., & Amara, A. 2013, The Astrophysical Journal, 780, 17, doi: [10.1088/0004-637X/780/1/17](https://doi.org/10.1088/0004-637X/780/1/17)
- N'Diaye, M., Pueyo, L., & Soummer, R. 2015, The Astrophysical Journal, 799, 225, doi: [10.1088/0004-637X/799/2/225](https://doi.org/10.1088/0004-637X/799/2/225)
- Nielsen, E. L., De Rosa, R. J., Macintosh, B., et al. 2019, The Astronomical Journal, 158, 13, doi: [10.3847/1538-3881/ab16e9](https://doi.org/10.3847/1538-3881/ab16e9)
- Otten, G. P. P. L., Snik, F., Kenworthy, M. A., et al. 2017, The Astrophysical Journal, 834, 175, doi: [10.3847/1538-4357/834/2/175](https://doi.org/10.3847/1538-4357/834/2/175)
- Pairet, B., Cantalloube, F., Gomez Gonzalez, C. A., Absil, O., & Jacques, L. 2019, Monthly Notices of the Royal Astronomical Society, 487, 2262, doi: [10.1093/mnras/stz1350](https://doi.org/10.1093/mnras/stz1350)
- Paszke, A., Gross, S., Massa, F., et al. 2019, in Advances in Neural Information Processing Systems, Vol. 32 (Curran Associates, Inc.)
- Paszke, A., Gross, S., Massa, F., et al. 2019, arXiv preprints
- Pedregosa, F., Varoquaux, G., Gramfort, A., et al. 2011, Journal of Machine Learning Research, 12, 2825
- Perrin, M. D., Sivaramakrishnan, A., Makidon, R. B., Oppenheimer, B. R., & Graham, J. R. 2003, The Astrophysical Journal, 596, 702, doi: [10.1086/377689](https://doi.org/10.1086/377689)
- Prusti, T., de Bruijne, J. H. J., Brown, A. G. A., et al. 2016, Astronomy & Astrophysics, 595, A1, doi: [10.1051/0004-6361/201629272](https://doi.org/10.1051/0004-6361/201629272)
- Pueyo, L. 2016, The Astrophysical Journal, 29
- Quanz, S. P., Schmid, H. M., Geissler, K., et al. 2011, The Astrophysical Journal, 738, 23, doi: [10.1088/0004-637X/738/1/23](https://doi.org/10.1088/0004-637X/738/1/23)
- Racine, R., Walker, G. A. H., Nadeau, D., Doyon, R., & Marois, C. 1999, Publications of the Astronomical Society of the Pacific, 111, 587, doi: [10.1086/316367](https://doi.org/10.1086/316367)
- Rameau, J., Chauvin, G., Lagrange, A.-M., et al. 2013, Astronomy & Astrophysics, 553, A60, doi: [10.1051/0004-6361/201220984](https://doi.org/10.1051/0004-6361/201220984)
- Ren, B., Pueyo, L., Zhu, G. B., Debes, J., & Duchêne, G. 2018, The Astrophysical Journal, 852, 104, doi: [10.3847/1538-4357/aaa1f2](https://doi.org/10.3847/1538-4357/aaa1f2)
- Ribak, E. N., & Gladysz, S. 2008, Optics Express, 16, 15553, doi: [10.1364/OE.16.015553](https://doi.org/10.1364/OE.16.015553)

- Ribeiro, M. T., Singh, S., & Guestrin, C. 2016, in Proceedings of the 22nd ACM SIGKDD International Conference on Knowledge Discovery and Data Mining (San Francisco California USA: ACM), 1135–1144, doi: [10.1145/2939672.2939778](https://doi.org/10.1145/2939672.2939778)
- Ross, A. S., Hughes, M. C., & Doshi-Velez, F. 2017, arXiv:1703.03717 [cs, stat]. <http://ascl.net/1703.03717>
- Ruane, G., Ngo, H., Mawet, D., et al. 2019, The Astronomical Journal, 157, 118, doi: [10.3847/1538-3881/aafee2](https://doi.org/10.3847/1538-3881/aafee2)
- Ruffio, J.-B., Macintosh, B., Wang, J. J., et al. 2017, The Astrophysical Journal, 842, 14, doi: [10.3847/1538-4357/aa72dd](https://doi.org/10.3847/1538-4357/aa72dd)
- Samland, M., Bouwman, J., Hogg, D. W., et al. 2021, Astronomy & Astrophysics, 646, A24, doi: [10.1051/0004-6361/201937308](https://doi.org/10.1051/0004-6361/201937308)
- Schramowski, P., Stammer, W., Teso, S., et al. 2020, arXiv:2001.05371 [cs, stat]. <http://ascl.net/2001.05371>
- Simonyan, K., Vedaldi, A., & Zisserman, A. 2013, arXiv preprint arXiv:1312.6034. <http://ascl.net/1312.6034>
- Smilkov, D., Thorat, N., Kim, B., Viégas, F., & Wattenberg, M. 2017, SmoothGrad: Removing Noise by Adding Noise, arXiv. <http://ascl.net/1706.03825>
- Snik, F., Otten, G., Kenworthy, M., et al. 2012, in Modern Technologies in Space- and Ground-based Telescopes and Instrumentation II, Vol. 8450 (SPIE), 224–234, doi: [10.1117/12.926222](https://doi.org/10.1117/12.926222)
- Soummer, R., Pueyo, L., & Larkin, J. 2012, The Astrophysical Journal, 755, L28, doi: [10.1088/2041-8205/755/2/L28](https://doi.org/10.1088/2041-8205/755/2/L28)
- Sparks, W. B., & Ford, H. C. 2002, The Astrophysical Journal, 578, 543, doi: [10.1086/342401](https://doi.org/10.1086/342401)
- Stolker, T., Bonse, M. J., Quanz, S. P., et al. 2019, Astronomy & Astrophysics, 621, A59, doi: [10.1051/0004-6361/201834136](https://doi.org/10.1051/0004-6361/201834136)
- Sundararajan, M., Taly, A., & Yan, Q. 2017, in Proceedings of the 34th International Conference on Machine Learning (PMLR), 3319–3328
- Sutskever, I., Martens, J., Dahl, G., & Hinton, G. 2013, in Proceedings of the 30th International Conference on Machine Learning (PMLR), 1139–1147
- The Astropy Collaboration, Robitaille, T. P., Tollerud, E. J., et al. 2013, A&A, 558, A33, doi: [10.1051/0004-6361/201322068](https://doi.org/10.1051/0004-6361/201322068)
- The Astropy Collaboration, Price-Whelan, A. M., Sipőcz, B. M., et al. 2018, AJ, 156, 123, doi: [10.3847/1538-3881/aabc4f](https://doi.org/10.3847/1538-3881/aabc4f)
- The Astropy Collaboration, Price-Whelan, A. M., Lim, P. L., et al. 2022, ApJ, 935, 167, doi: [10.3847/1538-4357/ac7c74](https://doi.org/10.3847/1538-4357/ac7c74)
- Thompson, W., & Marois, C. 2021, arXiv:2103.09252 [astro-ph]. <http://ascl.net/2103.09252>
- Tobin, T. L., Currie, T., Li, Y., et al. 2024, The Astronomical Journal, 167, 205, doi: [10.3847/1538-3881/ad3077](https://doi.org/10.3847/1538-3881/ad3077)
- Vallenari, A., Brown, A. G. A., Prusti, T., et al. 2023, Astronomy & Astrophysics, 674, A1, doi: [10.1051/0004-6361/202243940](https://doi.org/10.1051/0004-6361/202243940)
- van der Walt, S., Schönberger, J. L., Nunez-Iglesias, J., et al. 2014, PeerJ, 2, e453, doi: [10.7717/peerj.453](https://doi.org/10.7717/peerj.453)
- van Leeuwen, F. 2007, Astronomy & Astrophysics, 474, 653, doi: [10.1051/0004-6361:20078357](https://doi.org/10.1051/0004-6361:20078357)
- Vigan, A., Fontanive, C., Meyer, M., et al. 2021, Astronomy & Astrophysics, 651, A72, doi: [10.1051/0004-6361/202038107](https://doi.org/10.1051/0004-6361/202038107)
- Virtanen, P., Gommers, R., Oliphant, T. E., et al. 2020, Nature Methods, 17, 261, doi: [10.1038/s41592-019-0686-2](https://doi.org/10.1038/s41592-019-0686-2)
- Wahhaj, Z., Cieza, L. A., Mawet, D., et al. 2015, Astronomy & Astrophysics, 581, A24, doi: [10.1051/0004-6361/201525837](https://doi.org/10.1051/0004-6361/201525837)
- Wang, J. J., Ruffio, J.-B., De Rosa, R. J., et al. 2015, Astrophysics Source Code Library, ascl:1506.001
- Waskom, M. 2021, JOSS, 6, 3021, doi: [10.21105/joss.03021](https://doi.org/10.21105/joss.03021)
- Wolf, T. N., Jones, B. A., & Bowler, B. P. 2023, Direct Exoplanet Detection Using Deep Convolutional Image Reconstruction (ConStruct): A New Algorithm for Post-Processing High-Contrast Images, arXiv. <http://ascl.net/2312.03671>
- Zúñiga-Fernández, S., Bayo, A., Elliott, P., et al. 2021, Astronomy & Astrophysics, 645, A30, doi: [10.1051/0004-6361/202037830](https://doi.org/10.1051/0004-6361/202037830)

## APPENDIX

## A. RESIDUAL NOISE DISTRIBUTION

A common assumption for the quantification of detections and non-detections in HCI is that the residual noise after post-processing with PCA is Gaussian distributed (see, e.g., Mawet et al. 2014). This assumption is generally justified by the central limit theorem (we average many frames along time) and the whitening effect of PCA. Nevertheless, the residual noise after post-processing often deviates from Gaussian noise (Pairet et al. 2019; Bonse et al. 2023). This is problematic because the risk of false positives (we claim a detection that is just noise) depends on the type of noise. More specifically, the probability of observing a value of  $S/N = 5$  that is just noise is higher if the noise is heavy-tailed, that is, the frequency of bright values such as speckles is higher than for Gaussian noise. Bonse et al. (2023) found that if the residual noise follows a Laplacian distribution, the final contrast could be overestimated by up to one magnitude if the test of Mawet et al. (2014) is used.

In practice, the true noise distribution is usually unknown, making it difficult to compare limits across datasets. This is also true if we want to compare different post-processing techniques. We study the residuals of PCA and 4S for the datasets #1–#9 (see Table 1) to get a better understanding of their noise distributions. The datasets #10 and #11 are excluded due to strong oversaturation at close separations. We consider two regions: 1. within  $2.5\text{--}4.5 \lambda/D$ , and 2. within  $5.0\text{--}7.0 \lambda/D$  distance to the star. For each dataset and region we, plot Q-Q plots and calculate the coefficient of determination  $R^2$  (see, e.g., Pairet et al. 2019 for a detailed explanation). A comparison of the residual noise for datasets #5 and #9 is shown in Figure 12. The Q-Q plots shown in the figure compare the pixel noise distribution with Gaussian noise. If the residual noise was perfectly Gaussian, we would expect all values to lie on the gray diagonal line. The better the observed noise can be explained by Gaussian noise, the closer the coefficient of determination  $R^2$  is to 1. For PCA, the large values are above the diagonal line, indicating that the noise is heavy-tailed. In the case of 4S, the residual noise is much closer to Gaussian, although it is still not perfectly Gaussian. The quantification based on the  $R^2$  values confirms this observation. A summary of the results for all datasets is shown in Figure 13. In general, the residual noise at close separations tends to be more affected by speckle and is therefore often more non-Gaussian. For most datasets, especially those for which PCA deviates the most from Gaussian noise, 4S improves the Gaussianity of the residuals. This means that 4S does not only improve the contrast limits as shown in Section 5, but also reduces the risk of false positives.

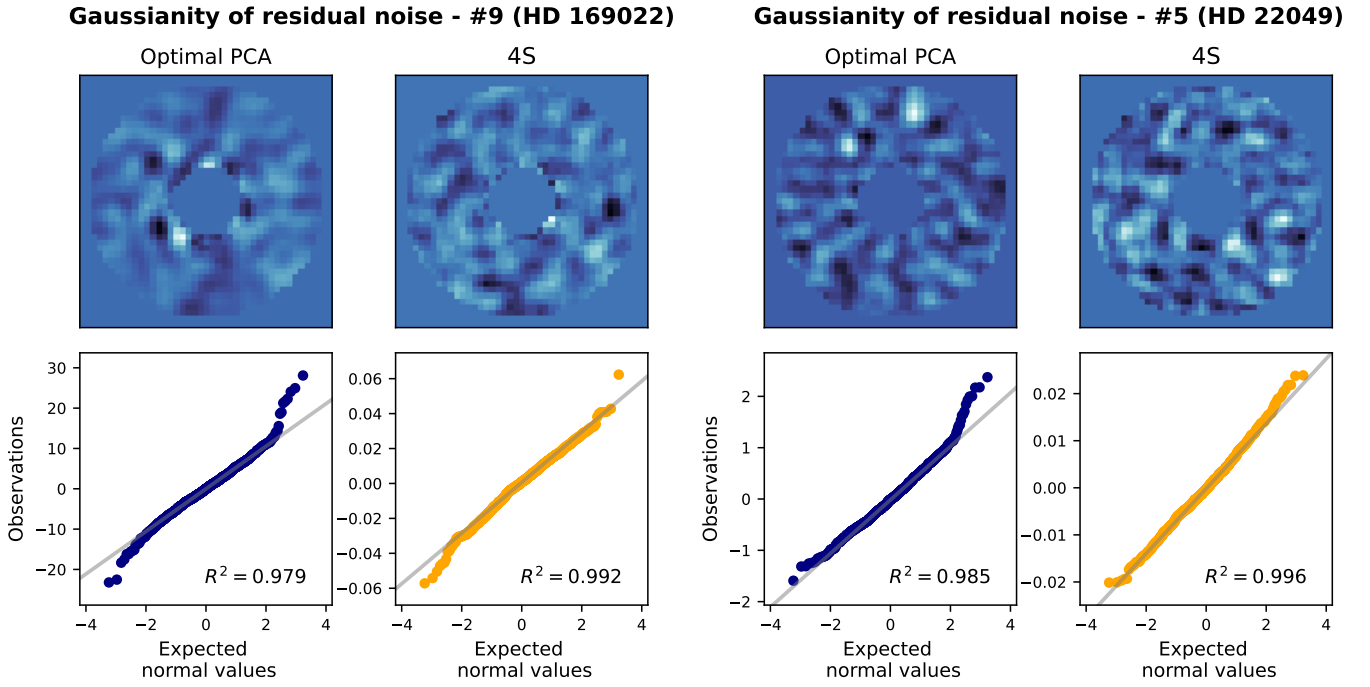


**Figure 12.** Two examples of the Gaussianity test performed in Figure 13. The top row shows examples of the residuals obtained with PCA and 4S. The pixels outside  $2.5\text{--}4.5 \lambda/D$  were masked to extract the noise. Q-Q plots are shown below. If the noise were perfectly Gaussian, we would expect all values to be on the gray diagonal line and the value of  $R^2$  to be close to 1.

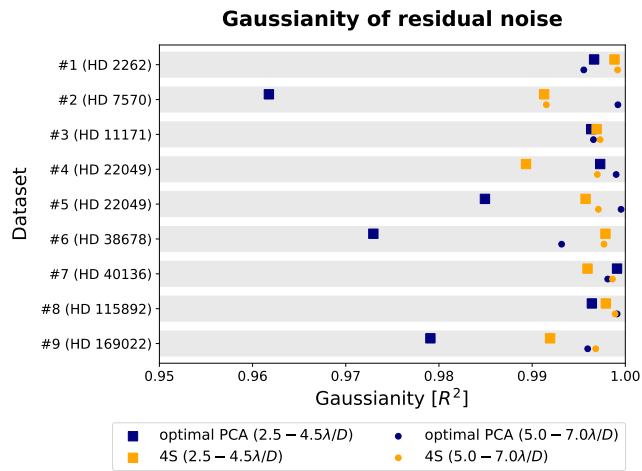


**Figure 13.** Comparison of the Gaussianity of the noise in the residuals of 4S and PCA for the datasets #1-#9. If the coefficient of determination  $R^2$  is closer to 1, the noise is better explained by Gaussian noise. We choose the number of principal components  $K$  and the regularization strength  $\lambda$  of 4S that maximizes the contrast (*optimal PCA*).



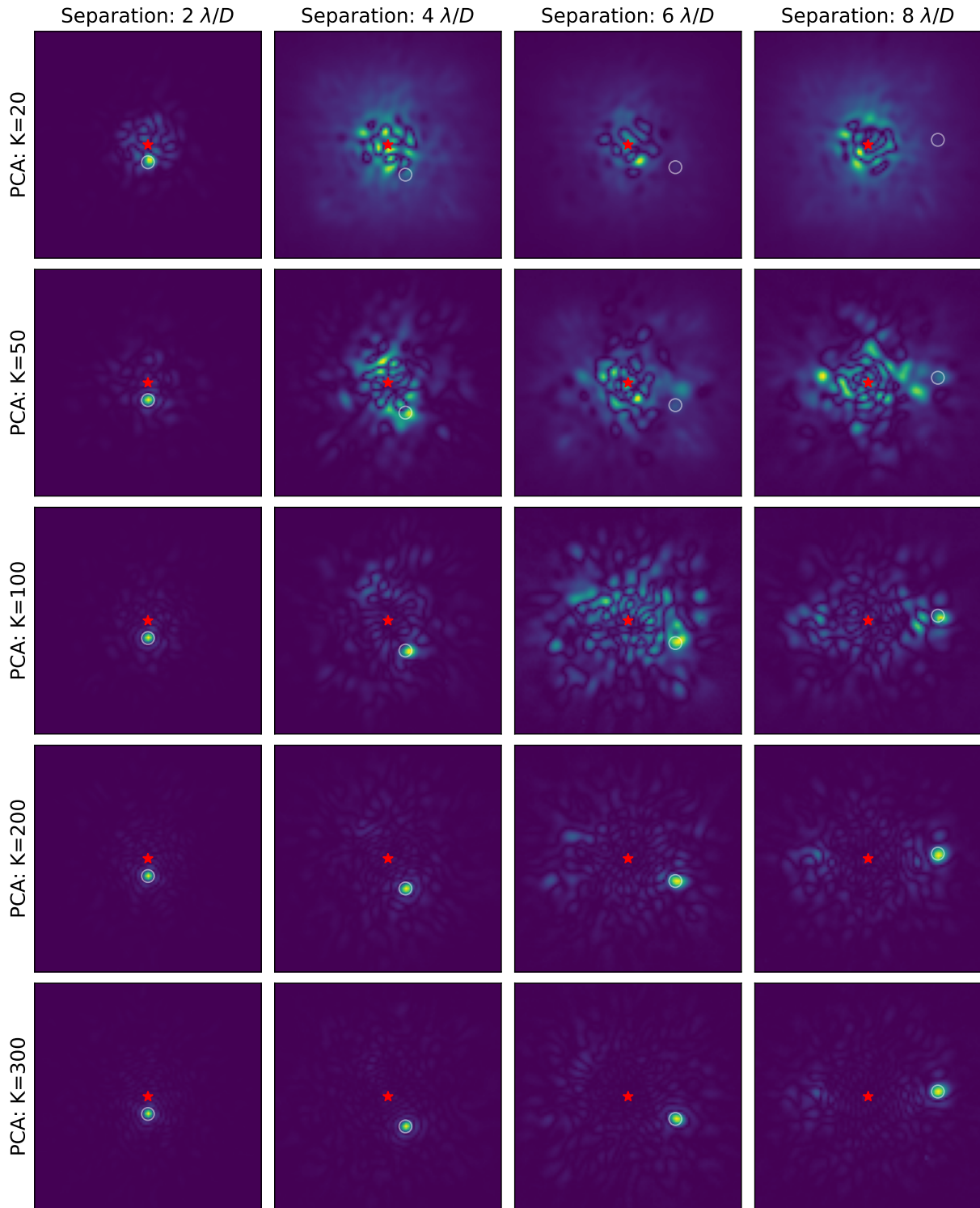


**Figure 14.** PCA saliency maps for different numbers of principal components  $K$  and separations from the star. The saliency maps show which information from the science frames is used by PCA to estimate the noise at the position marked by the white circle. Especially for large  $K$  and separations close to the star, only the information within the white circle is used, resulting in a substantial loss of the planet signal. The red star marks the center of the frame.

### Residuals - AF Lep b (2011)

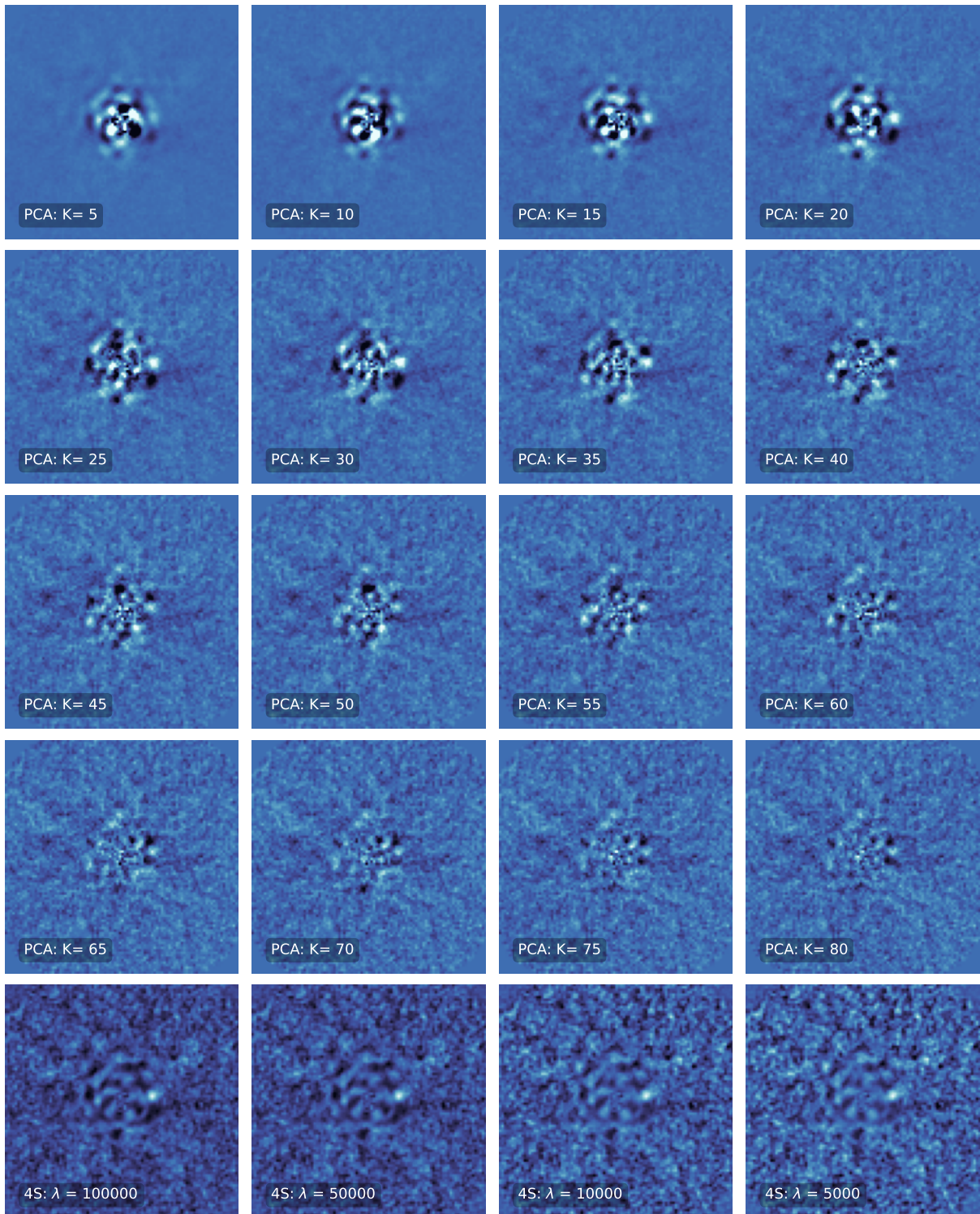


**Figure 15.** Residual images of the AF Lep dataset shown in Figure 10 for several different settings of the algorithm's hyperparameters (principal components  $K$  for PCA and regularization strength  $\lambda$  for 4S). The planet AF Lep b is barely visible in the PCA residuals. For 4S, any choice of parameters yields a clear detection, highlighting the robustness of the method.